Fall 2012

Development and quantitative assessment of a beam hardening correction model for preclinical micro-CT

Sucheta Mohapatra
University of Iowa

Recommended Citation

Mohapatra, Sucheta. "Development and quantitative assessment of a beam hardening correction model for preclinical micro-CT." MS (Master of Science) thesis, University of Iowa, 2012.
https://doi.org/10.17077/etd.su5a92a8

DEVELOPMENT AND QUANTITATIVE ASSESSMENT OF A BEAM HARDENING

CORRECTION MODEL FOR PRECLINICAL MICRO-CT

by

Sucheta Mohapatra

A thesis submitted in partial fulfillment
of the requirements for the Master of
Science degree in Biomedical Engineering
in the Graduate College of
The University of Iowa

December 2012

Thesis Supervisor: Associate Professor John J. Sunderland

Graduate College
The University of Iowa
Iowa City, Iowa

CERTIFICATE OF APPROVAL

_____

MASTER'S THESIS

_____

This is to certify that the Master's thesis of

Sucheta Mohapatra

has been approved by the Examining Committee
for the thesis requirement for the Master of
Science degree in Biomedical Engineering
at the December 2012 graduation.

Thesis Committee: _____
                  John J. Sunderland, Thesis Supervisor

                  _____
                  Joseph M. Reinhardt

                  _____
                  John E. Bayouth

Nothing in life is to be feared, it is only to be understood.

Marie Curie

ACKNOWLEDGMENTS

I am really grateful to my research advisor, Dr. John J. Sunderland. I appreciate his contributions of time, ideas, and funding to make my graduate study experience so productive and stimulating.

I would like to thank the personnel of Small Animal Imaging Core (SAIC) and PET Imaging Center - Susan Walsh, Christine Mundt and Michael Acevedo. It has been my privilege to work in such a dynamic environment and learn the diverse aspects of micro-CT operation in our facility. Special thanks to Dr. Shikui Yan of Siemens Medical Solution USA, Inc. Knoxville, TN, for his valuable inputs during this study.

I would like to thank my academic advisor, Dr. Joseph M. Reinhardt for his valuable support during the course of my study in Iowa. Thanks to Dr. John E. Bayouth, for taking the time and effort to be a part of my exam committee. Special thanks to the secretaries of Biomedical Engineering, Ms. Angela and Ms. April, for their generous help.

I owe my gratitude to Late Professor Geoffrey McLennan for providing me the opportunity to work at the TLIRP. His dedication towards research and his accomplishments shall continue to inspire me towards my future goals. I owe a lot to all my friends and colleagues in Iowa City, who have stood by me in the best and worst of times, and made my life here, a joyful and learning experience.

I am grateful to my parents, Sabita Mohapatra and Kailash Chandra Mohapatra, for their unflagging love and support, even when I am thousands of miles away. I am forever indebted to my father, who has spared no effort to provide me the best possible education despite all the hardships and financial constraints. Thanks to my brother, Shakti, who I grew up with a passion for Science. Finally, I am thankful to my beloved husband, Dr. Chandra Shekhar Mohapatra, for his unwavering faith in me, wealth of ideas, sparkling humor and for being the very special person that he is.

ABSTRACT

The phenomenon of x-ray beam hardening (BH) has significant impact on preclinical micro-CT imaging systems. The causal factors are the polyenergetic nature of x-ray beam used for imaging and the energy dependence of linear attenuation coefficient (μ) of the imaged material. With increase in length of propagation of beam in the imaged object, lower energy photons in the projected beam become preferentially absorbed. The beam "hardens" (as average energy increases) and progressively becomes more penetrating, causing underestimation of the linear attenuation coefficient. When this phenomenon is not accounted for during CT reconstruction, it results in images with non-uniform CT number values across regions of uniform density. It leads to severe errors in quantitative applications of micro-CT and degradation in diagnostic quality of images. Hence, correction for beam hardening effect is of foremost importance and has been an active area of research since the advent of μ-CT [2][3][4].

The Inveon™ μ-CT system uses a common *linearization* approach for BH correction. It provides a set of standard default coefficients to be applied during CT reconstruction. However, our initial experiments with uniform water phantoms of varying diameters indicated that the correction coefficients provided by default in the Inveon™ system are applicable for imaging mouse-size (~28 mm) objects only. For larger objects the correction factors yielded incorrect CT values along with characteristic 'cupping' observed in the uniform central region of the phantom.

This study provides an insight into the nature and characteristics of beam hardening on the Inveon CT system using water phantoms of varying sizes. We independently develop and assess the performance of a beam hardening correction method based on linearization using cylindrical water phantoms of two different diameters - [Φ = 28 mm and Φ = 71 mm]. The selected diameters represent mouse and rat sizes respectively. The measured non-linear relationship between beam attenuation and

length of propagation is fitted to a polynomial function, which is used to estimate the effective mono energetic attenuation coefficient (μ_{eff}) for water. The estimated μ_{eff} value is used to generate the expected sum of attenuation coefficients along each x-ray path through the imaged object. The acquired poly-energetic data is then linearized to expected projections using a third order polynomial fit, which is consistent with the Inveon™ BH model and software. BH correction achieved with the proposed model demonstrates effective removal of the characteristic cupping artifact, that was observed when Siemens *default* BHC coefficients were applied. In addition to water phantoms, we also test the effectiveness of the proposed scheme using solid cylindrical phantoms of three different densities and composition. The proposed method was also used to measure the BH effect for 12 different kVp/filtration combinations. By generating twelve distinct sets of BHC coefficients, for each setting, we achieve a significant expansion in the quantitative performance of the Inveon CT system.

TABLE OF CONTENTS

LIST OF TABLES

LIST OF FIGURES

x

CHAPTER 1
INTRODUCTION

1.1 Motivation

This study was conducted on the high resolution Siemens Inveon™ μCT system, capable of generating CT images with 20 μm resolution. When properly calibrated, the system is designed to provide quantitative images with individual pixel values in Hounsfield units, just as in human CT scanners.
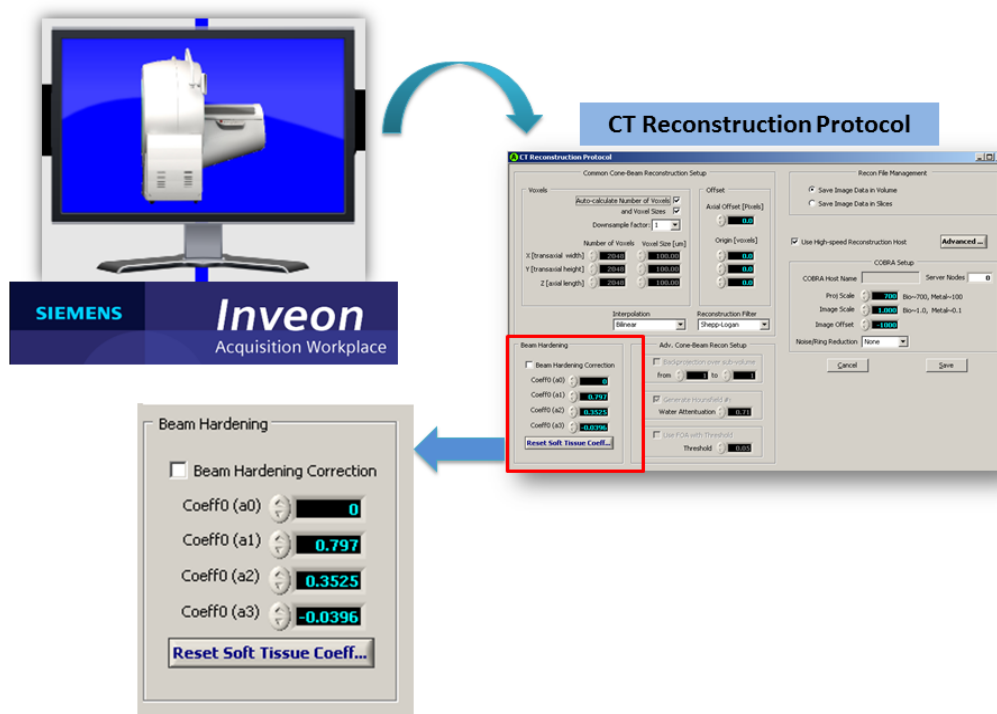
Figure 1.1 The Inveon μCT Reconstruction protocol. The red highlight shows the polynomial based BH correction coefficients built-in the system and used as default. [Image Source: The Inveon Acquisition Workflow (IAW) System]

To ensure accurate quantitation, the Inveon CT reconstruction protocol provides a built-in application for beam hardening (BH) correction, as shown in Fig 1.1. When the BH correction is selected by the user, a third-degree polynomial-based soft tissue beam hardening correction is applied directly to the CT projection data. This pre-reconstruction correction process is based on the principle of *linearization*, which was first described by *Brooks and Di Chiro* in their seminal paper in 1975.

In our initial experiments we imaged uniform cylindrical water phantoms of four different diameters - 15mm, 28mm, 50mm and 71mm. The image acquisition parameters used were 80 kVp, 500 μ A, 360 degrees rotation, 120 views with 0.5 mm Al equivalent of additional tube filtration.

The CT projection data for each phantom was reconstructed in two ways:

1) Without using any correction for beam hardening

2) By using the default beam hardening correction coefficients built in the Inveon™ CT.

Line profiles were drawn axially across the central region of the CT images of each phantom and the results were displayed **[Fig 1.3-Fig 1.6]**. It was observed that:

- The axial profile diagrams with no BH correction showed significant 'cupping' artifacts for all phantom sizes.

- Application of default BH correction coefficients during reconstruction helped to reduce the 'cupping' artifact in the central region of images.

- However, the extent of correction achieved with the default correction method was found to depend on size of the object, which should not be the case when an accurate beam hardening correction is implemented in a system. The correction was found to be adequate for phantom diameters up to about 28 mm **[Fig 1.3, 1.4].** However, for larger sizes of phantoms equivalent to rat-size (up to 71 mm), severe depression could be observed resulting in a "cupping" appearance. **[Fig 1.2, 1.5, 1.6]**
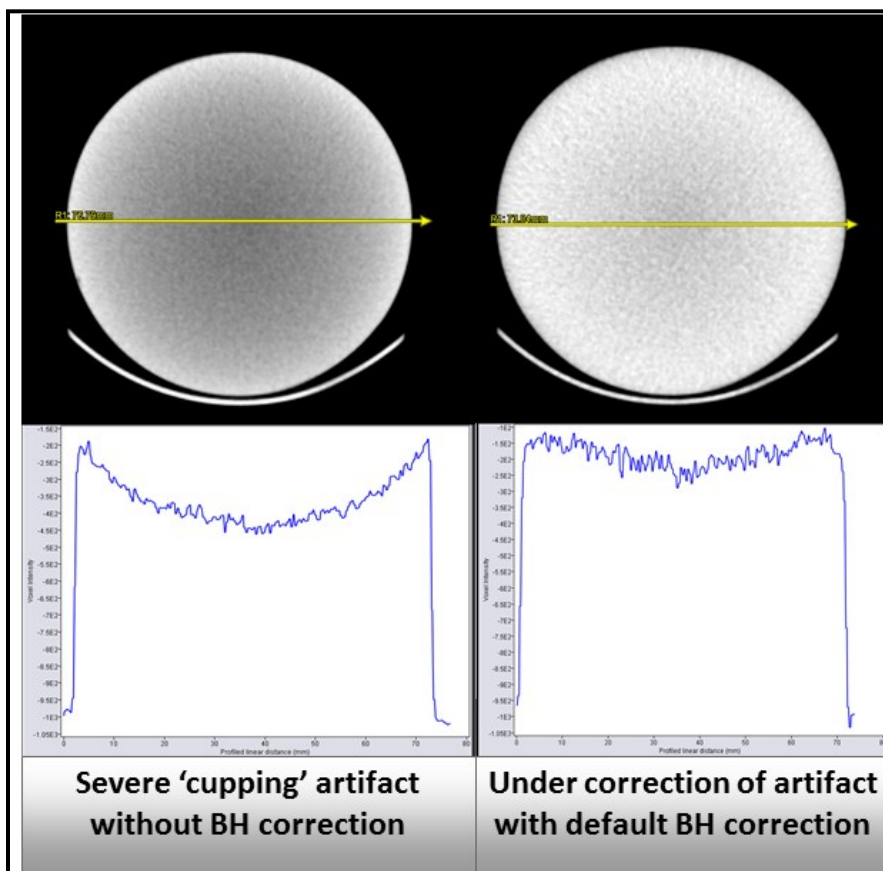
Figure 1.2 Reconstructed image profiles of 71 mm diameter water phantom

These findings clearly indicated serious impact on quantitative CT measurements induced due to errors from inadequate beam hardening corrections. Recognizing the limitations of the Inveon™ CT system with regard to beam hardening correction gave rise to the need to undertake an in-depth study of the process of beam hardening and the correction mechanism implemented by Siemens. The investigation was deemed particularly important due to the fact that the same CT measurements are used to generate attenuation correction values for quantitative PET imaging.
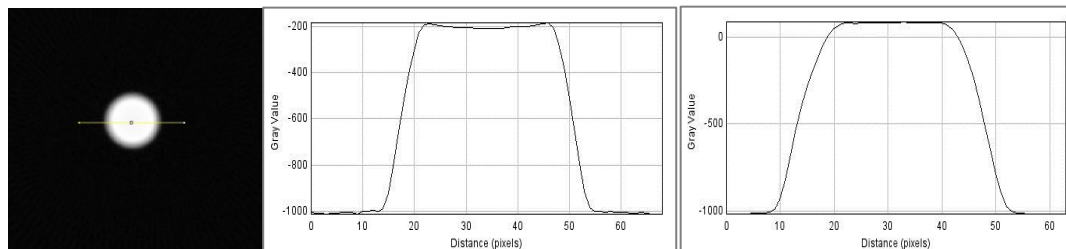
Figure 1.3 Reconstructed CT line profile diagrams for 15 mm diameter phantom.
- Left -   When no BH correction is applied
- Right - BH correction with default coefficients
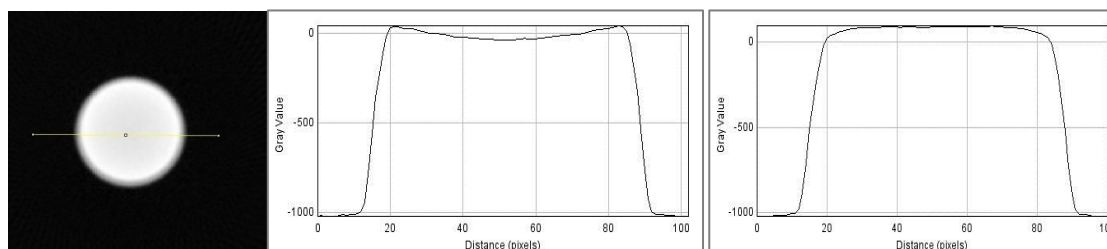
Figure 1.4 Reconstructed CT line profile diagrams for 28 mm diameter phantom.
- Left - When no BH correction is applied
- Right – BH correction with default coefficients
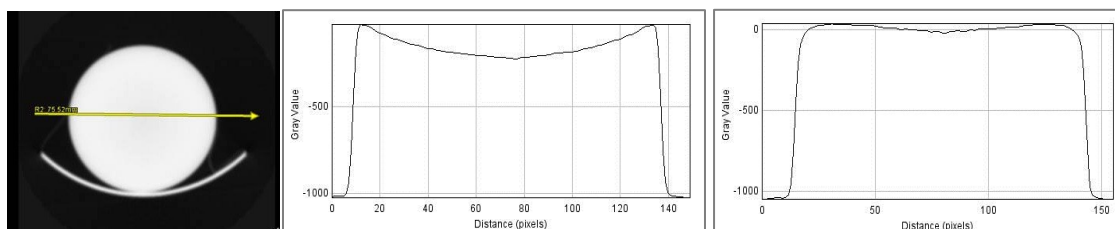
Figure 1.5 Reconstructed CT line profile diagrams of 50 mm diameter phantom.
- Left- When no BHC is applied
- Right - BHC with default coefficients showing a slight residual cupping artifact
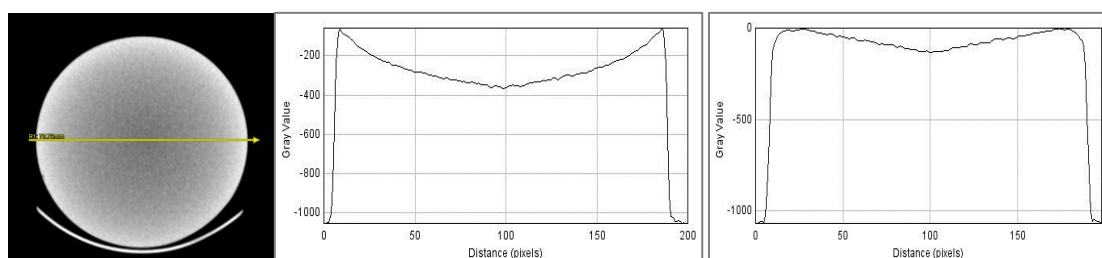
Figure 1.6 Reconstructed CT line profile diagrams of 71 mm phantom.
- Left - When no BH correction is applied
- Right – BH correction with default coefficients shows significant cupping artifact.

1.2 Objectives and Scope

This study was undertaken to both understand and correct the preliminary observations discussed in the previous section. In particular, the specific objectives and scope of the work described in this thesis were as follows:

- Achieve a detailed understanding of the causes and effects behind the phenomenon of beam hardening for various materials with different densities observed within the realm of cone beam micro-computed tomography.

- Understand the *linearization with polynomials* correction technique, which forms the underlying principle of BH correction, implemented by Siemens on the Inveon microCT system.

- Model and develop an independent methodology for derivation of coefficients of the polynomial used for correction of beam hardening within the context of the Inveon system. Quantitative evaluation of the accuracy of the developed approach was done by phantom studies. Uniform cylindrical water phantoms of varying sizes were imaged using an array of commonly used kVp and filtration combinations and the beam hardening characteristic curves were determined as accurately as possible. Additionally, materials with higher densities like Aluminum, Polyoxymethylene (POM) and Polyethylene were tested to assess the efficacy of the methodology.

- Assure that our newly derived beam hardening correction parameters result in uniformly accurate quantitative reconstructions independent of object size.

CHAPTER 2
THEORY & BACKGROUND

2.1 Why is the X-ray Spectrum Poly-energetic?

In commercial medical imaging systems, x-rays are produced when fast moving electrons are rapidly decelerated by a metal target. In its simplest form, an x-ray tube is a large vacuum tube containing a heated tungsten filament cathode and a tungsten alloy anode. When heated to incandescence, the cathode emits a cloud of electrons that are subsequently accelerated towards the anode operating at a high positive voltage. The interaction of the high energy electrons with the anode material results in the production of x-rays (discussed in detail below). The anode is designed to direct the collimated x-rays toward an object to be imaged. The frequency of the emitted photons, and therefore their energy, is dependent on the amount of kinetic energy of the incident electrons, which in turn, is dependent on the applied potential difference between the anode and the cathode.

The interaction between the high-energy electrons and the anode results in two independent x-ray production mechanisms. The predominant mechanism is due to inelastic scattering of the impinging electrons onto the anode target nuclei. The kinetic energy of electrons is lost by deflection due to the electrostatic braking force by the positively charged atomic nuclei on the negatively charged electron, and manifests as x-ray photons. The degree of deceleration is different depending upon the closeness of approach of the electron to the nucleus and the resulting angle of deflection, resulting in a continuous spectrum of energies emitted. This process is known as "*Bremsstrahlung radiation*". The maximum *Bremsstrahlung* photon energy corresponds to the kinetic maximum energy of the incident electrons that is equal to the potential difference applied between the anode and the cathode.
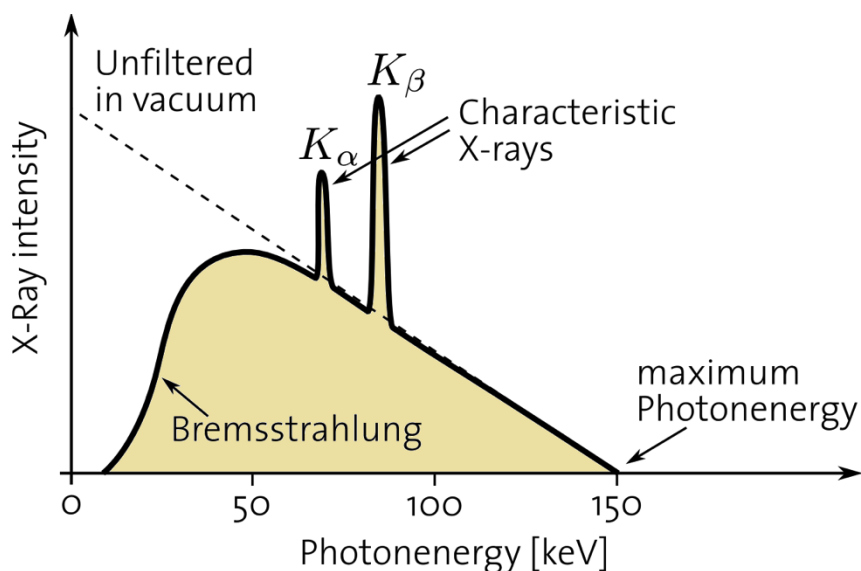
Figure 2.1 Shows the X-ray continuous spectrum and characteristic peaks Characteristic X-rays have discrete energy values represented by vertical peaks, while Bremsstrahlung X-Rays are continuous and can have any energy level up to the maximum that the x-ray system is set to. [3]

The second type of x-ray producing interaction is *"characteristic"* x-ray radiation, which is observed as additional set of discrete peaks (K_α, K_β), superimposed on top of the Bremsstrahlung radiation curve. These peaks result from collisions between the high-energy electrons accelerated from the cathode and inner shell electrons in the target (anode) atoms. The collision results in the ionization of the target atom, and a subsequent x-ray photon cascade. The interaction can occur only if the incoming electron has a kinetic energy greater than the binding energy or excitation potential of the electron within the atom. An electron in higher energy state drops down to fill the 'hole' created in the lower energy state, emitting an x-ray photon. The emitted x-ray photon has energy equal to the difference between the upper and lower energy levels of the electron that filled the core gap.

The resulting x-ray spectrum is therefore a *polychromatic beam,* consisting of a mixture of characteristic and bremsstrahlung radiation. Low energy x-rays below approximately 20 keV are mostly absorbed by the x-ray tube; added filtration in the form of thin pieces of metal is often put in the photon path to preferentially absorb additional lower energy photons that are of no use in the imaging process. The maximum energy of the x-ray produced is equal to the maximum potential applied across the x-ray tube. This peak x-ray energy is usually described with the unit- kVp (peak voltage). A change in kVp changes the accelerating potential between anode and cathode. Hence it affects both the number of photons (quantity) and the maximum energy (quality) of the x-ray emission spectrum as shown in Fig. 2.2
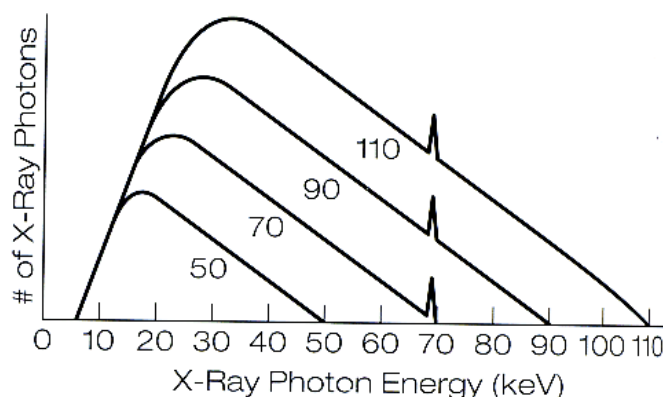
Figure 2.2   Schematic illustration of effect of change in peak voltage on the emission spectrum. Note that both the quantity and quality of x-ray photons increase with increase in kVp, whereas position of characteristic peaks do not change. [3]

2.2 Attenuation of X-Rays

2.2.1 The Linear Attenuation Coefficient (LAC)

As the beam of x-rays propagates through the imaged object, they are primarily attenuated by absorption (due to the photoelectric effect) and scattering (Compton scattering). The basic equation for the total attenuation of a monoenergetic beam through a homogeneous material is given by Beer's Law:

$$I = I_0 \exp\left[-\mu.\Delta x\right] \qquad (2.1)$$

Where I_0 is the incident x-ray intensity, μ is the linear attenuation coefficient (LAC) for the material being scanned (units: 1/length), and Δx is the length of the x-ray path through the material. If the scan object in the path of x-ray is composed of 'n' different materials, the equation is represented as:

$$I = I_0 \exp\left[\sum_{i}^{n}(-\mu_i \Delta x_i)\right] \qquad (2.2)$$
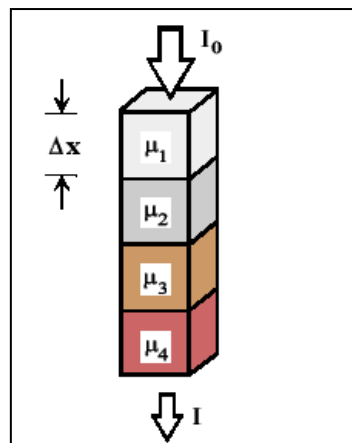
Figure 2.3 Illustration of Beer's Law for a non-homogenous object

Each increment in *i* reflects a single material with attenuation coefficient μ_i over a linear extent x_i. This is analogous to a monoenergetic x-ray photon beam passing through a narrow column of tissue of variable composition. It is more prevalent to express distances in terms of product of density ρ and thickness *x*. The beam transmission equation (2.1) can then be rewritten as:

$$I = I_0 \exp\left[-\left(\mu/\rho\right).\rho x\right] \tag{2.3}$$

where μ/ρ is called the *mass attenuation coefficient*, which in contrast to the linear attenuation coefficient does not depend on the density of the absorber, but only on its composition.

2.2.2 Energy Dependence of LAC

From the standpoint of medical imaging the following interactions of x-rays with matter are pertinent:

- Photoelectric effect
- Compton scatter

The total, *linear attenuation coefficient µ* of a material, at a given beam energy is given by the following sum:

$$\mu_{total} = \mu_{photoelectric} + \mu_{scatter} + \mu_{pair\ production} \tag{2.4}$$

For the given range of photon energies commonly encountered in diagnostic imaging, i.e 20–140 keV, the mechanisms primarily responsible for x-ray beam attenuation are – photoelectric absorption and compton scatter. Photoelectric absorption

consists of complete absorption of the energy of the incident x-ray photon by a tightly bound inner shell electron. The electron uses some of this energy to overcome the binding energy and the rest manifests as its kinetic energy as it escapes the parent atom. Compton scattering occurs when x-ray photon interaction occurs with loosely bound outer shell electrons, resulting in partial loss of photon energy and deflection of path of photon travel. As shown in Fig 2.4, the probability that a photon will undergo photoelectric absorption or Compton scattering, depends primarily on the incident photon energy (E) and the composition of the material (atomic number Z). It is observed that in high Z materials such as bone, photoelectric effect is dominant at the lower energies. The LAC for such materials decreases rapidly with increasing energy due to its photo electric component ($\mu_{photoelectric} \sim Z^3/E^4$). On the other hand, the Compton scatter component of LAC undergoes gradual decrease with increase in both photon energy and atomic number of material.
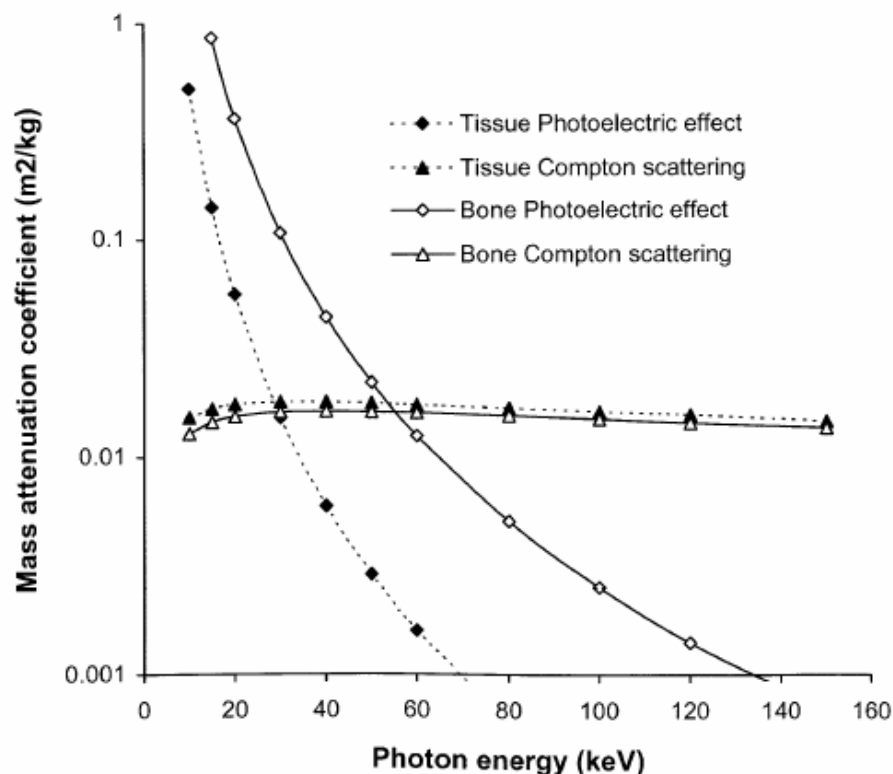
Figure 2.4 Energy dependence of mass attenuation coefficient. Within the energy range of diagnostic imaging, the number of photons interacting through the photoelectric effect decreases rapidly with photon energy, while the probability of Compton scattering is largely independent of energy. [6]

2.3   The CT Projection Data

When a beam of x-ray passes through the imaged object, it is exponentially attenuated by the material along its path. The actual attenuation is not only dependent on the material but also on the energy spectrum of the x-ray source. The energy-dependent material constant that appears in the exponent of attenuation formula is called the *linear attenuation coefficient*   (μ cm^{-1}) of the material. It represents the fraction of radiation that is attenuated per unit distance through the material. Hence the total attenuation, which can be mathematically represented by a line integral, reflects the sum of all the local

linear attenuations along the path of the x-ray beam passing in a straight line through the object.

For tomographic imaging, a set of projections across the linear extent of the object is required from multiple angles. The x-ray projections of a 2D object is the set of line integrals at a given angle of the source around the axis of rotation. A diagram of a single projection at given angle θ is shown below in Figure 2.5.
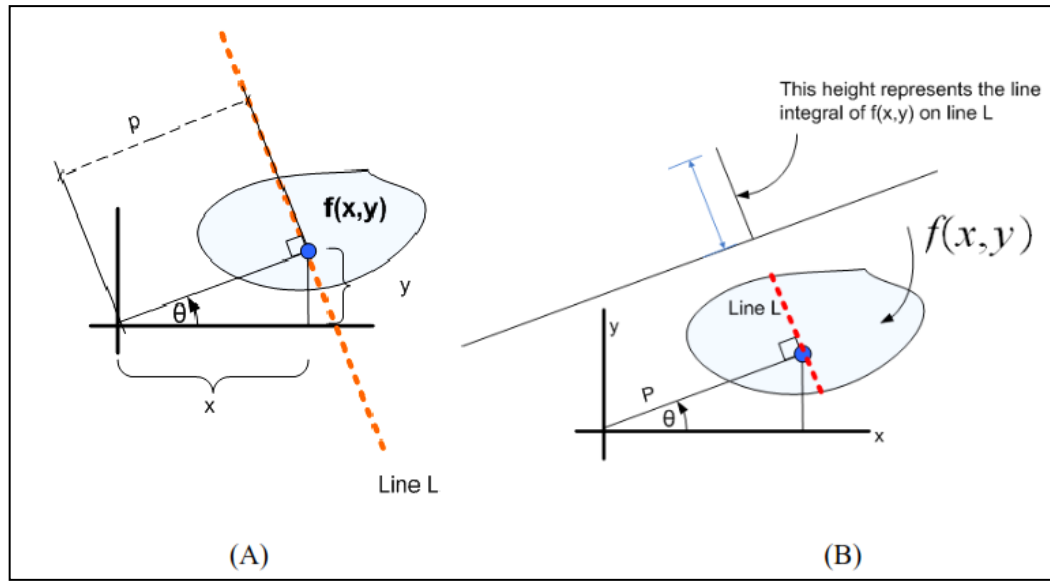
Figure 2.5 Radon Transform: Representation of CT projection [26]

Mathematical Definition: To mathematically express CT projection data, we consider Fig 2.5(A) where a beam of x-ray passes through a 2D object f(x,y) in the spatial domain. The coordinate origin is taken to be the axis of rotation of the source. Any point (x, y) on the line L with specific p and specific θ satisfies the following:

$$x\cos\theta + y\sin\theta = p \qquad (2.5)$$

If f(x,y) is defined over a region as in Fig. 2.5B, the integral of this function over (L, θ) will be expressed by use of Dirac delta function δ as below :

$$g(p,\theta) = \iint f(x,y)\delta(x\cos\theta + y\sin\theta - p)dxdy \qquad (2.6)$$

The function g(p, θ) is known as the *Radon Transform* of f(x,y). For a given θ, a complete set of line integrals recorded by a row of detectors, constitutes an x-ray projection.
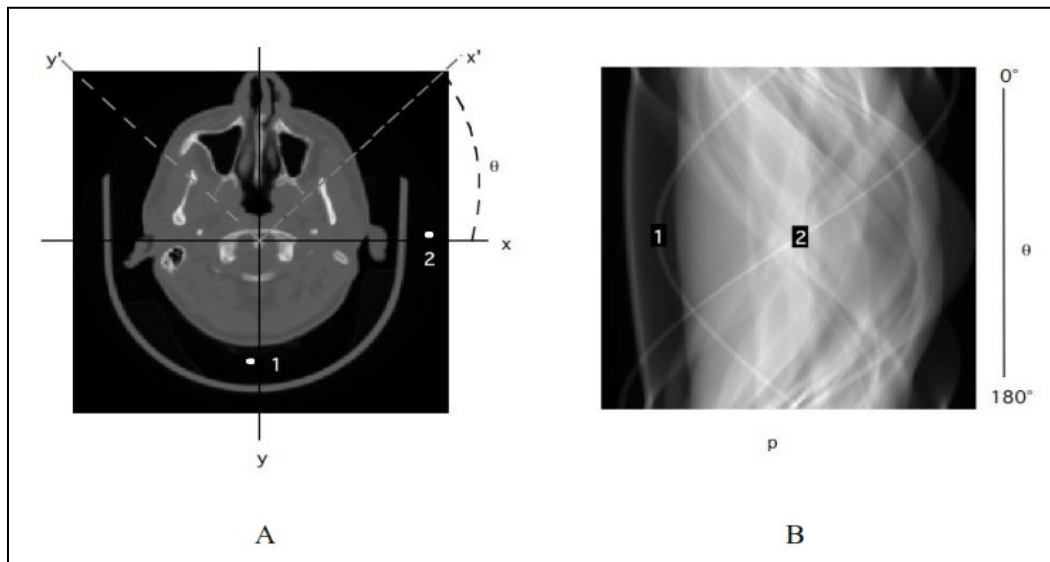
Figure 2.6 A) Object f(x,y) **B)** projections g(p, θ) represented as a 2D matrix called sinogram. Landmarks (1) and (2) indicate positions within a given projection angle The amplitude of each sinusoid in g(p, θ) is equal to its distance from the axis of rotation in f(x,y). [13]

A two-dimensional representation of the Radon transform is also known as a *Sinogram*. Fig 2.6 B illustrates the set of projections g(p, θ) for θ = 0º (top row) to θ = 180º (bottom row) from the CT image in 2.6 A. Columns (p) indicate positions within a given projection angle. Any given point on object f(x,y), which is not situated on the axis of rotation, follows a sinusoidal path on the sinogram g(p, θ). This can be seen by mapping the position of markers (1) and (2) between the two images A and B.

Mathematical Correlation between acquired CT raw data and CT projection*:* In reality, the raw projection data collected by the detector elements are the intensity of the x-rays transmitted through the object denoted by I(r). This acquired data must conform to the definition of projection as specified by Eq 2.6. Therefore, this quantity is modeled to represent a proper set of line integrals summing attenuation values. This is shown as below:

$$I_\theta(r) = I_0(r)e^{\iint -\mu(x,y)\delta(r - x\cos\theta - y\sin\theta)dxdy} \qquad (2.7)$$

Where I_θ (r) is the intensity detected at 'r' at projection angle θ and I_0(r) is the intensity at 'r' without the object in the scan field of view. Dividing both sides of the above equation by I_0(r) and taking the natural logarithm yields the following for the integral of linear attenuation coefficient.

$$-\ln\frac{I_\theta}{I_0} = \iint \mu(x,y)\delta(r - x\cos\theta - y\sin\theta)dxdy \qquad (2.8)$$

Combining Eq 2.6 and Eq 2.8 results in the following equation:

$$g(p,\theta) = -\ln\left(\frac{I_\theta}{I_0}\right) \tag{2.9}$$

Eq 2.9 shows that an x-ray CT image is a map or distribution of computed values of linear attenuation coefficients µ(x,y), which reflect the proportion of X-rays scattered or absorbed as they pass through each voxel location.

2.4 Image Reconstruction
2.4.1 For Parallel Beam Geometry

A number of methods exist by which the CT projection data g(p, θ) can be converted into an image f(x,y). But the most common approach used is *Filtered Back Projection (FBP)*. As the name suggests, it consists of two steps – filtration of projection data followed by backprojection. A simple back projection operation implies propagating the measured sinogram back in to image space along the projection paths. Mathematically,

$$f_{BP}(x,y) = \int_0^\pi p(x\cos\theta + y\sin\theta, \theta)d\theta \tag{2.10}$$

The final image is then taken as the sum of all backprojected views. However, as shown in Fig 2.7, this method has an inherent blurring effect. This effect can be understood by observing that by using simple backprojection as a reconstruction methodology, a single point in the true image is reconstructed as a radial function that decreases in intensity away from the center - i.e the point spread function of a simple back projection is circularly symmetric function that decreases as the reciprocal of its radius.

Mathematically, this effect can be represented as the result of a convolution between measured projection P, with a blurring function (1/r).

$$P_{measured} = P.\frac{1}{r} \tag{2.11}$$
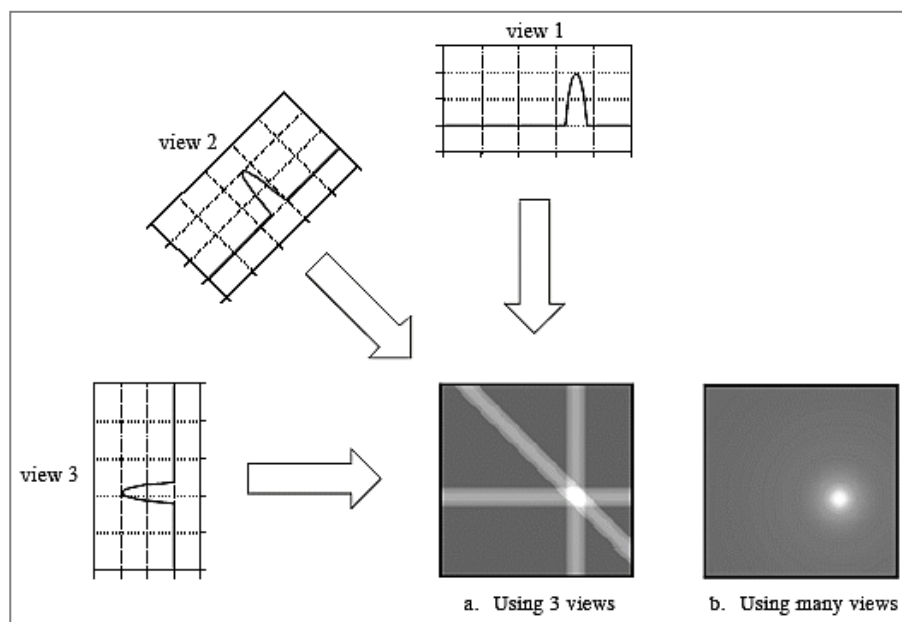
Figure 2.7 Shows radial blur effect of simple backprojection without prefiltering [18]

The radial blurring problem which is inherent in simple back projection is mathematically compensated using filtering techniques. Therefore, the overall reconstruction process is then called Filered Back Projection (FBP). In FBP, each of the views is convolved with a one dimensional filter kernel. Filter is designed to account for the backprojection blurring effect to create a set of 'filtered views'. Each filtered view is then back projected to obtain the correct image.

Considering Eq 2.11, taking Fourier transform on both sides:

$$F\left(P_{measurred}\right) = F(P).F\left(\frac{1}{r}\right)$$
(2.12)

F(1/r) is the mathematical representation of a ramp filter. Hence, corrected projection is obtained by inverse transform (IFT) of the result of division of measured projection by ramp function in fourier space.

$$P_{corrected} = IFT\left[\frac{F\left(P_{measured}\right)}{F\left(\frac{1}{r}\right)}\right]$$
(2.13)
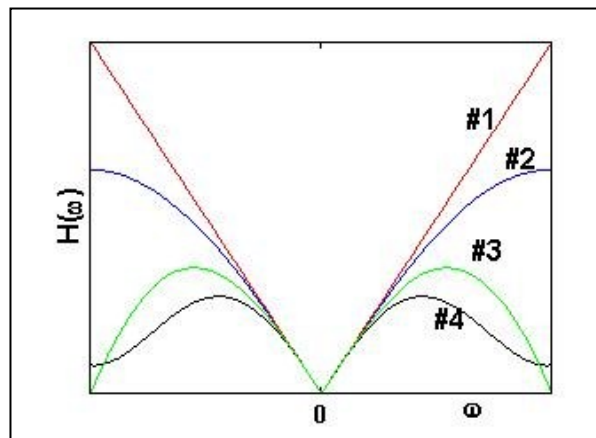
Figure 2.8 Magnitude response of different back projection filters: #1 = Ramp, #2 = Shepp-Logan, #3 = Cosine, #4 = Hamming. [19]

By multiplying the standard mathematically correct ramp function with a second filter function such as the Shepp-Logan, Hamming or Butterworth filter, it is possible to simultaneously correct the blurring effect and also enhance or suppress certain higher frequency (usually noise) features in the final back-projected image.

<u>2.4.2 For Cone Beam Geometry</u>

As compared to the simple parallel projection beam geometry, cone beam tomography has the advantages of simpler and faster data collection with less exposure to radiation. Fig 2.9 shows the cone beam geometry with a circular trajectory of the source and the area detector (Y, Z) around the object of interest (x, y, z).

A CBCT acquisition geometry is illustrated in Fig 2.9. Projection data is acquired as the photon beam from the x-ray source (apex) is incident on the detector (base), after passing through the imaged object. The axis of rotation (z-axis), of the source-detector system passes through the object and is perpendicular to the mid- plane which contains the source. Due to the cone beam nature, a series of tilted planes of projections are formed, relative to this mid-plane. Based on this geometry, Feldkamp *et al* derived the first fully three-dimensional reconstruction algorithm for cone beam geometry in 1984. The algorithm has since been popularly known as the FDK algorithm, and is widely used in clinical and industrial CBCT imaging applications [11]. Firstly, the area detector is scaled and translated to a plane which is parallel to it and also contains the axis of rotation Z as shown.
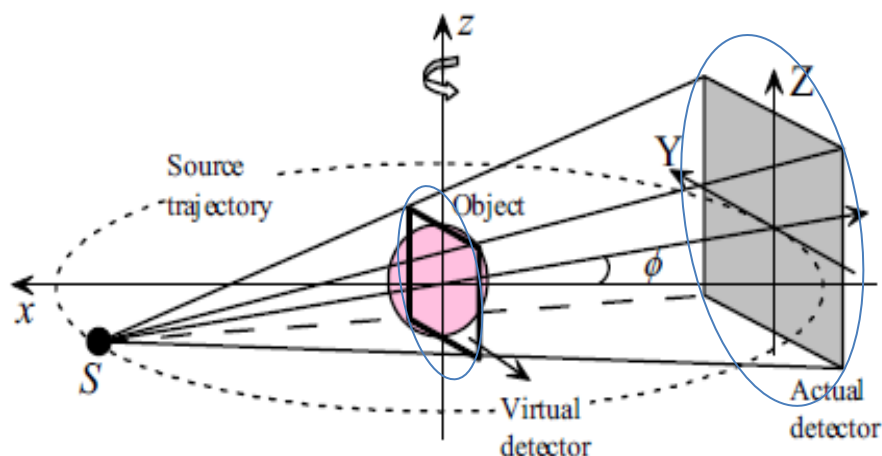
Figure 2.9 Illustration of projection on area detector in cone beam geometry [26]

Evidently, the projection data at the intersection of mid plane and the scaled detector plane (at z = 0) is applicable for fan-beam reconstruction formula. As a heuristic extension to the fan beam formula, in the cone beam case, the projection at the intersection of the detector plane with a tilted plane, can be regarded as belonging to a plane parallel to the mid plane (at z= non zero constant). This is equivalent to rotation of source along a circular path contained in the tilted plane. Radon transform for each such tilted plane is determined for a complete set of projection angles Φ. Convolution and weighted back projection is performed along each such plane. Details of derivation of the reconstruction formula are further described in [11].

The drawback associated with FDK algorithm is that when the source moves along the trajectory, the rotation angle increment ϕ is different from the midplane to the tilted planes. Hence, for large cone angles, the FDK algorithm suffers from an intensity drop for voxels away from the midplane. However, the reconstruction would be exact in the mid-plane (z = 0). Thus, the FDK algorithm is approximate in nature and as a

consequence, this is best suited for single-circular source trajectory and small cone angles [11] [15] [16]. Certain acquisition conditions, like insufficient number of projections (under sampling), limited scan angle, tend to produce severe image artifacts and hence requires exact algorithms. The reasons behind the popularity of the algorithm, despite its approximate nature, is its relative easy implementation, and its modest computational requirements.

2.5 Overview of Preclinical Imaging with Micro-CT

Small animals, particularly genetically engineered mice, are often used to create models of human diseases. Preclinical imaging systems provide a platform for *in vivo* studies of such small animals, which aid in gaining insight into disease biology and novel therapeutic options. The early nineties saw the development of the first micro-CT scanner by Feldkamp *et.al* [11]. Since then, the technique has evolved to become an invaluable research tool for capturing anatomical information of small laboratory animals down to the micron domain.

As compared to clinical CT scanners, preclinical micro-CT systems are designed and set-up for modeling *in-vivo* studies with rodents and small animals and typically provide very high spatial resolution images of tissues with high natural contrast, such as for bone and lung. In micro-CT, the source-detector pair consists of an x-ray tube delivering a cone beam of x-rays and CCD detector or camera. The detector is a 2D matrix covering the field of view in both axial and transaxial directions. This makes 3D imaging possible with only a single scan.

Micro-CT offers three options for imaging set-up - a rotating tube-detector pair as seen in clinical CT **(Fig. 2.10A)**, or a rotating specimen holder with static tube-detector unit **(Fig. 2.10B)**. The latter offers better stability and enhanced resolution. Compared to clinical CT, which are typically fan-beam systems with one-dimensional detectors, micro-CT systems employ cone-beam geometry based on an x-ray source and a two-dimensional detector (CCD camera) **(Fig. 2.10C)**.
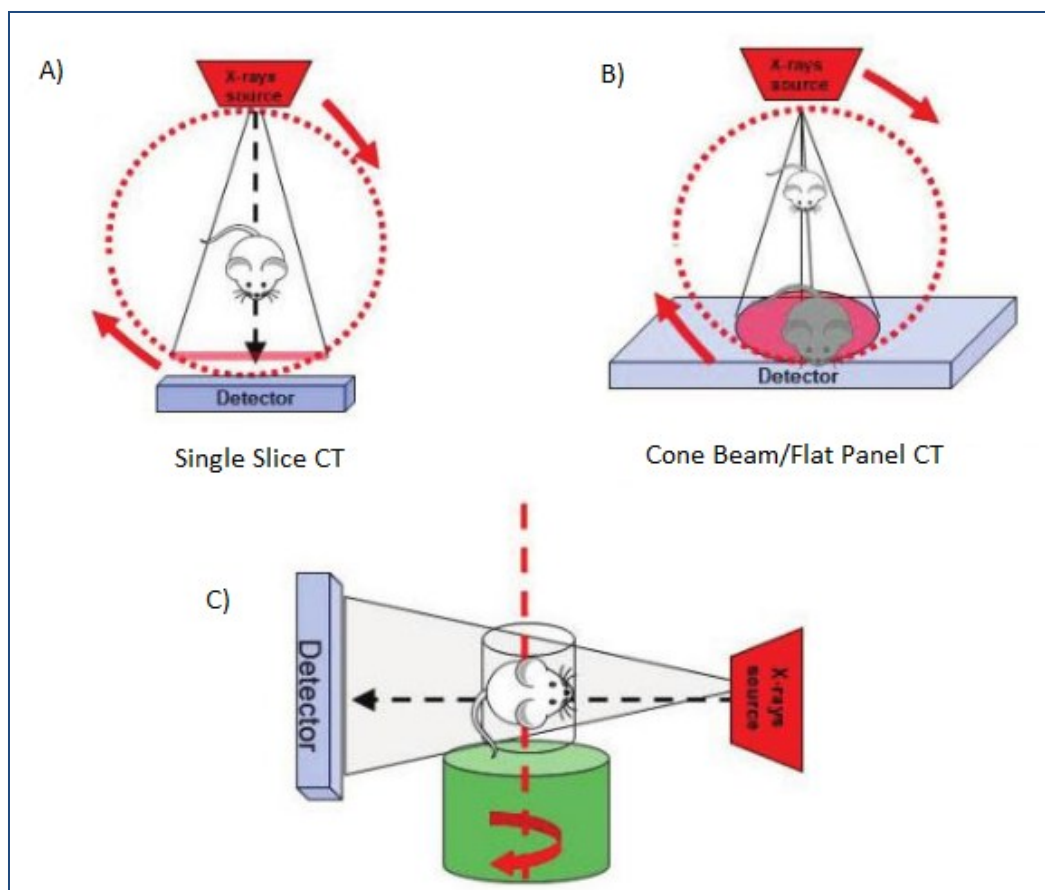
Figure 2.10 Shows different micro-CT configurations for imaging animal models. In systems A and B, the subject is placed in the center of the set-up and the gantry carrying the detector and x-ray source is rotated around it. A) shows a fan-shaped beam system with a single-slice detector and B) shows cone beam system fitted with flat panel detector. In the system (B), the specimen is placed on a stand that rotates within its own axis in the course of the beam. [10]

2.5.1 Flat Panel Detectors

In the development of cone beam micro-CT for small-animal imaging, two types of large area flat-panel detectors (FPDs) have been playing a crucial role. Image generation with flat-panel detectors is almost a real-time process, with a time lapse between exposure and image display of less than 10 seconds. Consequently, these systems are highly productive and increase throughput.

a) *Indirect Type* – Indirect FPDs are the most widely used sensors. It uses an X-ray scintillator optically coupled to a two dimensional array of amorphous silicon TFT/ photodiodes. The most commonly used scintillators are thallium-doped cesium iodide (CsI) , which converts the absorbed x-ray energy into visible light photons and pass it to the photodiode-TFT array. Each photodiode in the matrix is charge-coupled to a TFT, forming an individual pixel element. The striking photons produce electron-hole pairs in the photodiode layer. Activated pixels produce the electronic data which is represented as CT image. The type of detector used with the **Inveon μ-CT** system is indirect detection type. [Refer Sec 4.1]

b) *Direct Type* – As compared to an indirect detection type, the direct conversion FPD has a one step process. It utilizes an efficient layer of amorphous Selenium (a:Se), which converts incident photons directly into electrical charge. The electrical signal is carried out by a matrix of TFT which is charge-coupled to the detector layer.
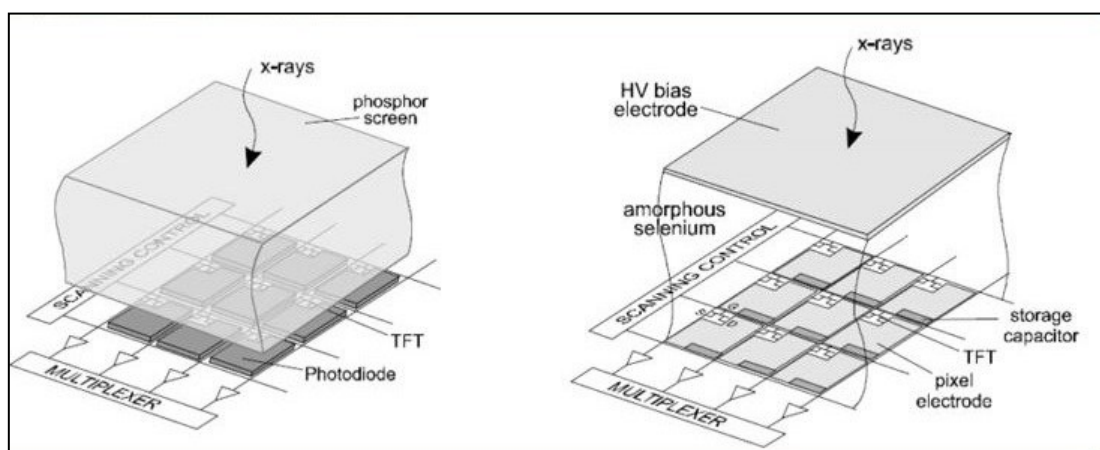
Figure 2.11 Two dimensional flat panel detectors for cone beam micro-CT: (On left) Indirect storage type. (On right) Direct photoconductor TFT type. [27]

2.6 The Beam Hardening Artifact

As discussed in section 2.4, the CT projection data is the result of interaction between the x-rays used for imaging and the materials constituting the imaged object. The basic principle of x-ray CT imaging is based on modeling this interaction by measuring the integrals of the attenuation coefficient (μ) of the x-ray beam as it travels through the object. A single projection is therefore, the sum of line integrals of the attenuation coefficient of the imaged material.

2.6.1 Single Energy Photon Transmission

For a homogenous material of uniform density, the linear attenuation coefficient μ is invariant with respect to voxel position. Let the projection obtained, with a monoenergetic x-ray source be represented as $R_{mono.}$ As defined by Beer's law, the line integral of x-ray attenuation is the log of the ratio of monochromatic x–ray photons that enter the object to those leaving the object. This can be derived as follows:
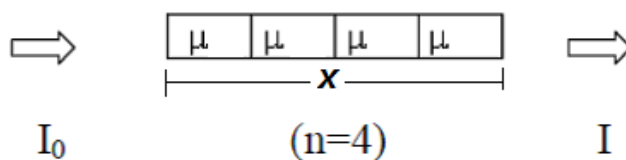
Considering 'n' pixels of width 'dx' in the path of each ray in a projection, the Beer-Lambert's law can be expressed in simplified way as:

$$I = I_0 \exp[-(\mu.ndx)] \qquad (2.14)$$

Solving Eq. 2.14, we get

$$I = I_0 \exp[-(\mu x)] \tag{2.15}$$

Thus, value of projection R_{mono} may be represented as below:

$$-\ln\left(\frac{I}{I_0}\right) = \mu \; x \tag{2.16}$$

$$R_{mono} = \mu \; x \tag{2.17}$$

It is important to note that, under the assumption that the beam is mono energetic, the value of R_{mono} (= μx), varies linearly with material thickness 'x' as μ remains constant for each voxel along the path.

2.6.2 Polyenergetic X-Ray Spectrum

When the incident beam is polyenergetic, the Beer Lambert's equation [Eq 2.15] no longer holds. This is because of the energy dependence of linear attenuation coefficient. Hence for a polyenergetic beam, the transmitted spectrum intensity could be represented as:

$$S_{exit}(E) = \int S_{in}(E) \exp\left(-\int \mu(E)dx\right)dE \tag{2.18}$$

where $S_{in}(E)$ represents the incident spectral energy density. In the energy ranges used for diagnostic examinations, the linear attenuation coefficient for tissues decreases with increasing energy [Sec.2.2.2]. In practice, the photons at the lower end of poly energetic spectrum are preferentially absorbed by the first few mm of material they pass through - primarily due to photoelectric effect. This results in the remaining beam becoming proportionally richer in high-energy photons. Therefore, the average energy associated with the exit spectrum $S_{exit}(E)$, becomes higher than the incident spectrum.

This phenomenon where the average energy of incident beam goes on increasing as it traverses through matter is called ***Beam Hardening.*** Beam hardening is a significant complicating factor in CT scanning because the average energy of an x-ray beam is dependent upon the amount of tissue it traverses. More tissue leads to higher average energy (due to selective absorption of lower energy photons). Thus, a higher average energy will result in lower calculated μ in those x-ray paths that traverse longer path-lengths. This effect is illustrated in Figure 2.12.

Significance of BH Correction - As a result of beam hardening, the non-linear relationship between CT attenuation and the length of x-ray propagation, manifests as shadow or 'cupping' artifact in a uniform homogenous medium. The measured μ-values are enhanced at the edges while they are underestimated at the center of the same medium. In case of multi-material objects, BH effect is observed as 'streaking' artifacts i.e. presence of dark streaks in between denser structures. Beam hardening in CT images makes the derivation of quantitative information not only difficult, but also meaningless. Hence, compensating for beam hardening is of primary importance for ensuring accuracy in quantitative CT.
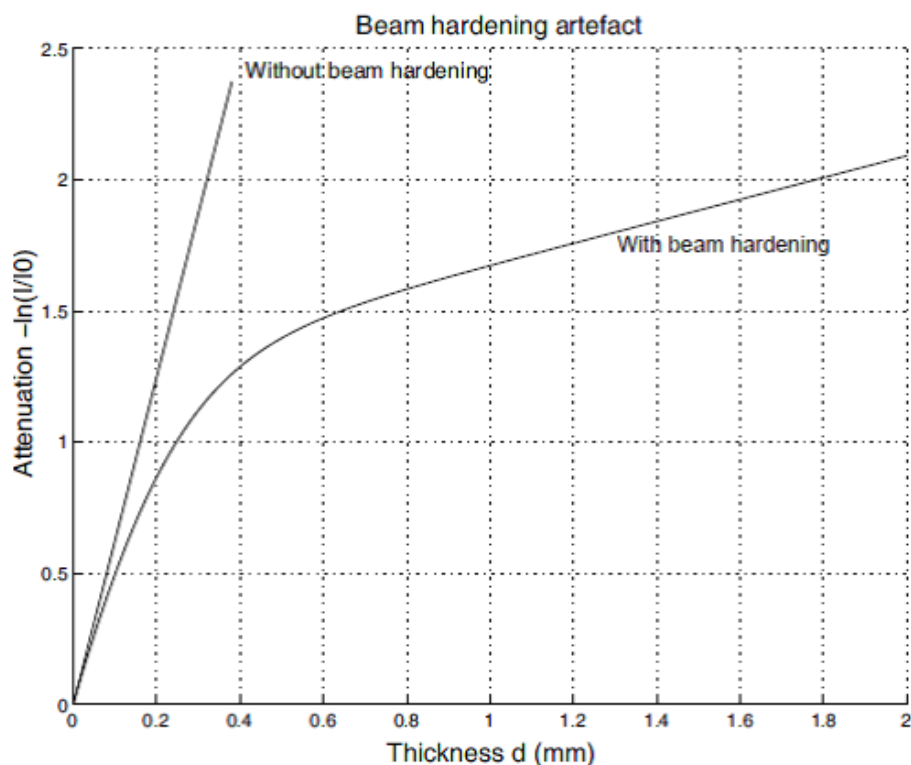
Figure 2.12 The straight line with constant slope represents the ideal linear relation between thickness and beam attenuation, assuming that the average beam energy remains constant through the material. Due to the effect of beam hardening, a nonlinear relation is observed between the material thickness d irradiated by a polyenergetic x-ray beam and the attenuation. The nonlinear curve shown in this graph has been obtained for Al at a peak voltage of 80 kVp. [11]

CHAPTER 3

COMMON TECHNIQUES OF BEAM HARDENING CORRECTION

In this chapter, we review some of the important and most common beam hardening correction techniques. The significance of beam hardening correction is validated by the vast amount of research in this field since the inception of computed tomography in the early 1970s. Originally, water bags were used in head scanners to reduce beam-hardening artifacts; using this technique the incident beam was effectively pre-filtered by the constant water length and reduced the problem to a scan of a single "effective material".

However, the use of water bags was cumbersome and it also required higher patient radiation doses. It was found to effectively eliminate soft-tissue beam hardening but could not eliminate the larger beam-hardening problem resulting from the unknown distributions of bone present in the scanned volume.

There are several methods that have been developed over the years to compensate for beam hardening effects, some being quite simple, but not terribly effective, while others are more accurate, but complex in their implementation.

1) *Tube Filtration*- Filtration of x-ray source is done to remove "soft" or lower energies in the primary spectrum. This is done by placing thin sheets of a metal, such as aluminum, between the x-ray source and the object so the lower energy x-rays can be preferentially absorbed from the primary beam. In this way a harder, less polychromatic, beam is incident on the object. The amount of both the inherent and the added filtration are stated in mm of Al or mm of Al equivalent. The thickness of filter material chosen is dependent on atomic numbers, kVp settings, and the desired filtration factor. Tube filtration does a fair job of lowering (but not eliminating) beam hardening effects by "pre-filtering" lower energy photons. This is illustrated below in Figure 3.1. However the primary use of filtration in an x-ray system is to lower the radiation dose to the patient, as

described below. Filtration of the low energy spectrum aids in minimizing radiation dose to the subject through the selective attenuation of those low energy x-rays that would have no chance of penetrating all the way through the subject. Added filtration generally does not affect the peak energy of the spectrum. The primary disadvantage of this technique is the selective suppression of lower energy x-rays that generally contribute contrast to the image. This decreases the usable x-ray intensity and diminishes the contrast between different materials [12]. Hence it is disadvantageous for observation of biological objects, which attenuate hard photons ineffectively. Additionally, spectrum filtering results in a decrease of the image signal-to-noise ratio (SNR). To have a SNR in the reconstructed CT image comparable with the one obtained without filtering, the scanning time or tube voltage has to increase.
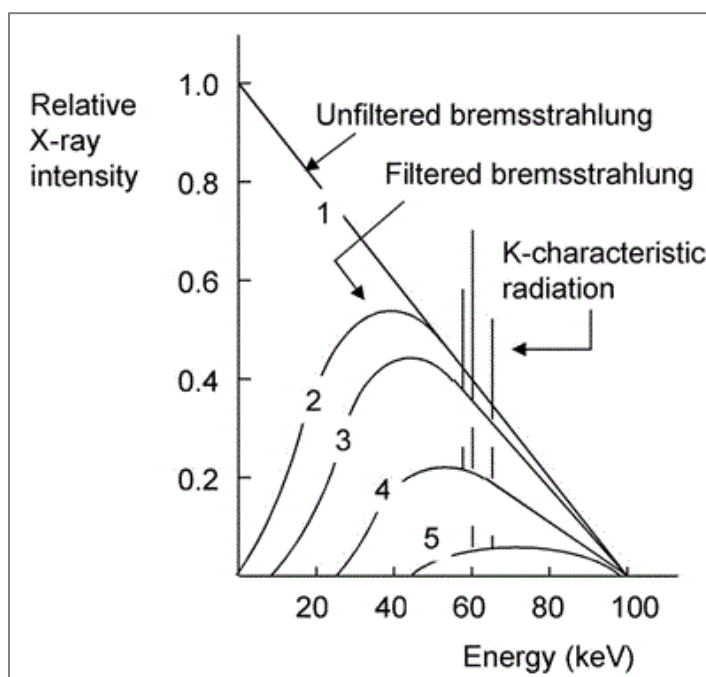
Figure 3.1 Shows added tube filtration results in increase in the average energy of the x-ray beam with an accompanying reduction in x-ray photon count [28]
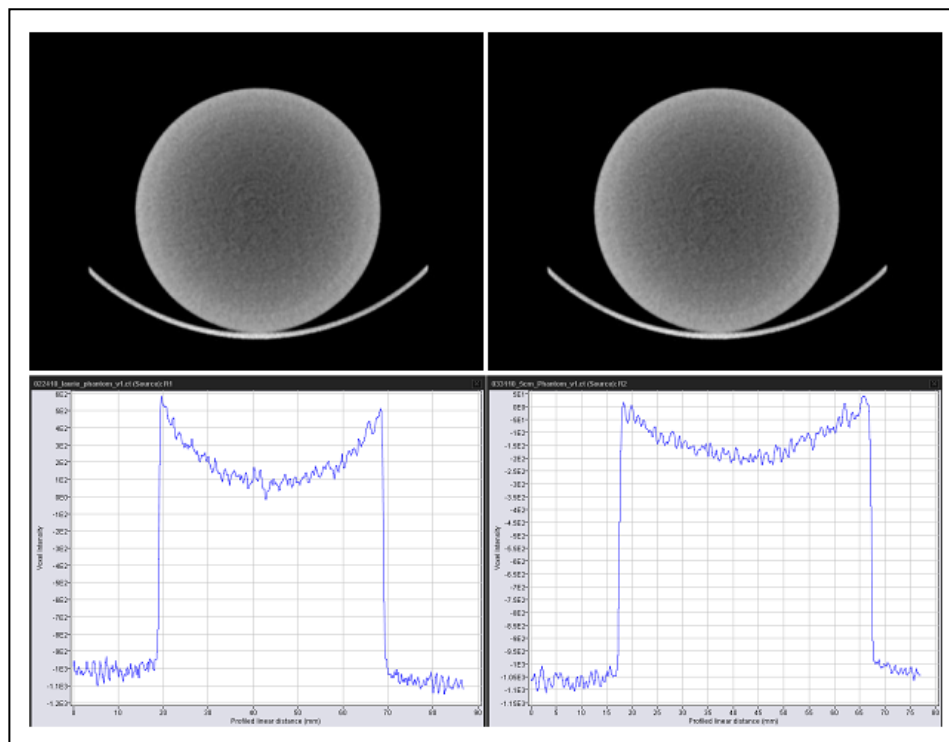
Figure 3.2 Radial profile diagrams of reconstructed CT images of uniform cylindrical water phantoms of diameter 28 mm. Reduction in cupping artifact can be observed on (B) as compared to (A) due to effect of 0.5 mm Al added tube prefiltration.
[Acquisition parameters: 80 kVp, 500 μA]

2) ***Dual Energy Method-*** *In* Dual-Energy CT (DECT), the imaged object is exposed to two different energy spectra or the data acquisition using special detectors with two different energy windows. The method was first popularized by R. Alvarez and A. Macowski (1976*).* Since projection data is acquired at two widely different energy levels the contribution of photoelectric and scatter effects are determined separately for each image pixel. Hence, the linear attenuation coefficient can be decomposed into two independent energy dependencies and two material selective images which can be combine BH artifact free images. This method is capable of eliminating beam-hardening artifacts [3] [10]. The disadvantage of this technique is its complexity and difficulty in implementation. It requires two consecutive exposures which increases scan time and dose. The

calibration procedure required to determine coefficients is prone to errors. The technique is also very sensitive to noise.

3) ***Statistical Correction Techniques*** - Statistical beam hardening reduction methods basically incorporate the polychromatic nature of the beam in a maximum likelihood (ML) algorithm. This approach assumes that the object consists of N known base substances, and that the energy dependence of the attenuation coefficient for each pixel can be described as a linear combination of the known energy dependencies of the base substances. Statistical methods are very flexible with respect to various geometries, prior knowledge, noise statistics, etc. However, such methods are computationally very expensive.

3.1 Linearization with Polynomials

The most common beam hardening correction implemented in commercial CT systems are based on linearization methods. Linearization methods aim to transform the measured polychromatic attenuation data into expected monochromatic attenuation data. This is one of the most commonly applied techniques to correct the non-linearities in CT images due to beam hardening [1-5]. As discussed earlier, beam hardening results in a non-linear relationship between measured attenuation and material thickness. The measured non-linear relationship between the polyenergetic case and the simpler monoenergetic case can be fit with a polynomial fitting function. Using this polynomial-based correction scheme the beam hardening can be compensated for, i.e. every value on the polynomial is corrected towards the linear plot which is expected in the monochromatic case [Fig 3.3]. According to The degree of polynomial is estimated depending on material density and severity of artifact *[Hammersberg and Mangard 1998]*
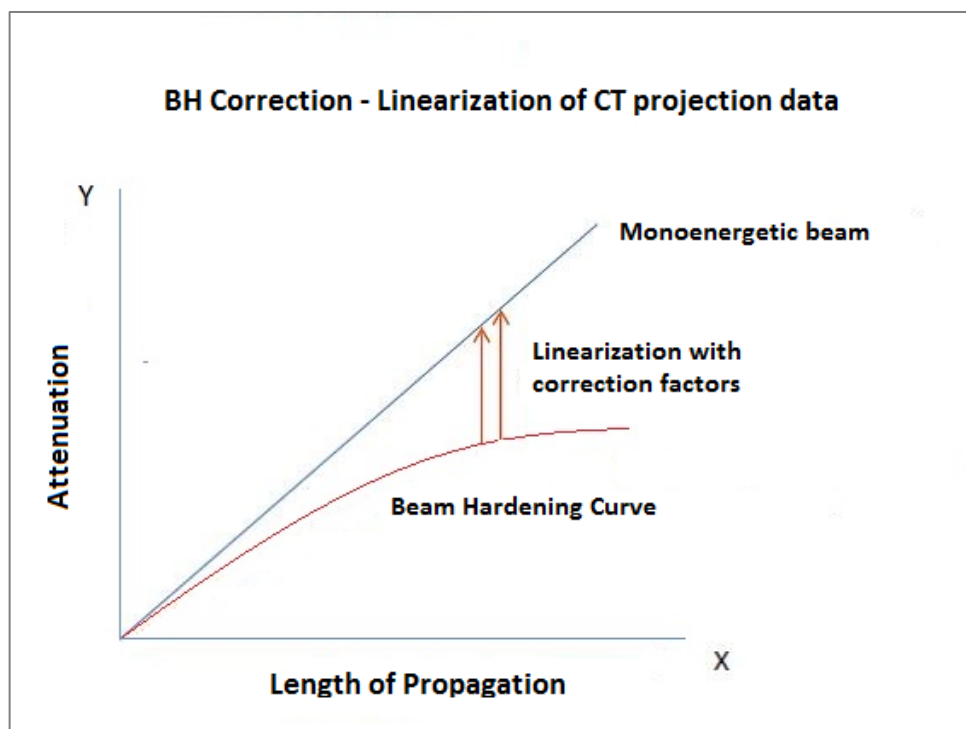
Figure 3.3 The process of linearization of polyenergetic projection data with correction coefficients.

This approach to BH correction is limited to single material objects with a homogenous composition only. However, because of the fact that murine subjects are of small size and their body composition predominantly consists of water and soft tissue (bone accounts for only a couple of percent of total body weight), the linearization technique is well-suited for BH correction in small animal x-ray imaging systems.

The Inveon micro-CT has implemented a linearization-based BH correction procedure using a third order polynomial function using water as the calibration material of choice. For multi-material objects, composed of widely different densities, this technique would result in non-uniform corrections and would generate quantitative anomalies in those areas with varying attenuation coefficients. However, as mentioned

previously, mice and rats are largely unit density animals and do not have the widely varying attenuation coefficients that would compromise effective use of this technique.

A second limitation of this method is that the linearization is usually performed for the entire region of x-ray detector, i.e. it does not include efficiency variations among detector pixels. Despite these drawbacks, the linearization approach to BH correction is by far the most commonly used approach in the industry.

CHAPTER 4

MATERIALS AND EXPERIMENTAL SET-UP

4.1 Overview of Inveon Micro-CT System
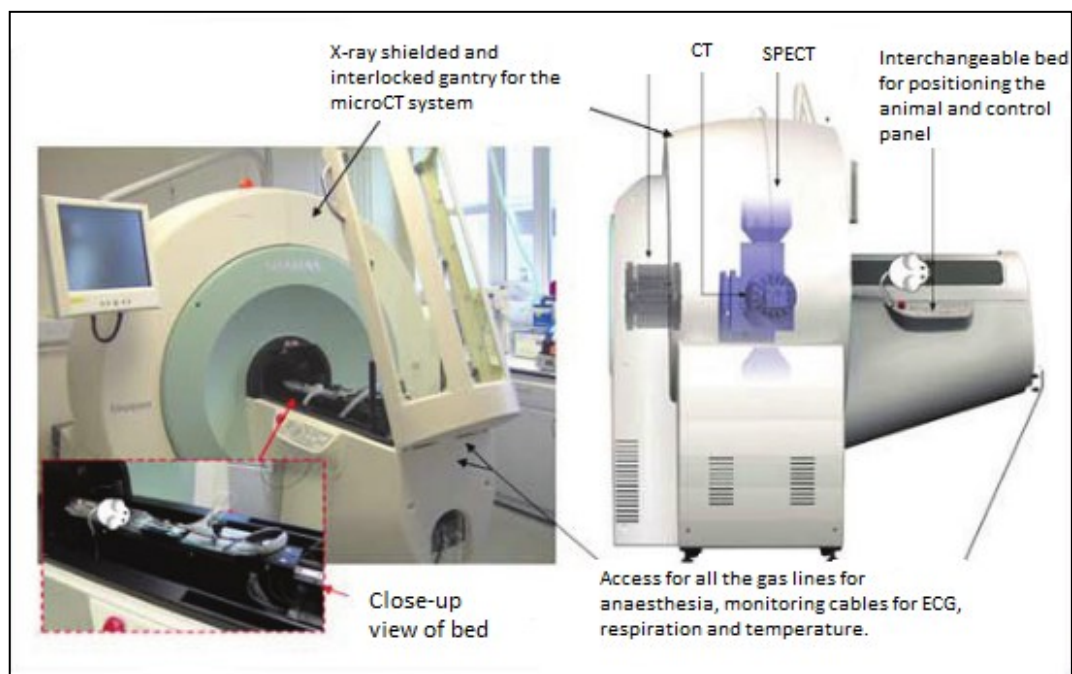
Figure 4.1 The Inveon preclinical µCT system.

The Inveon micro-CT system by Siemens consists of a standard x-ray source with a maximum power of 80 W, a peak voltage range of 40-80 kVp, and a tungsten anode having less than a 20 µm focal spot. The detection system is of indirect type. [Sec 2.3.1]. It is comprised of a gadolinium oxysulfide phosphor (Gd_2O_2S:Tb) scintillator screen (~thickness 25 µm), which converts incident x-ray photons to visible light photons. The CCD flat panel sensor is 125 mm wide, with 4096x4096 pixel elements (12-bit gray levels). Each detector element is approximately 30.5 μm in width. The maximum

achievable resolution with this detector and the standard X-ray source is close to 20 microns.

4.2 Description of Phantoms

To demonstrate the effect of beam hardening and to investigate the effectiveness of the correction approach, we considered five different kinds of uniform homogenous phantoms. Two of them were water-filled and the remaining three were solid phantoms. The constituent material, density and diameter of each phantom is cited in Table 4.1. The water phantoms are of primary interest, as they will generate the polynomial coefficients that will actually be used for beam hardening corrections on the animal models. The other materials were investigated to test the general applicability of our beam hardening correction approach.

Table 4.1 Description of phantoms used for experiment.

Phantom#	Material	Diameter (mm)	Density (g/cc)
1	Water-filled plastic cylinder	28	1.00
2	Water-filled plastic cylinder	71	1.00
3	Polyoxymethylene (POM) Delrin cylinder	26	1.410
4	Low Density Polyethylene (LDPE) cylinder	26.7	~ 0.97
5	Aluminum cylinder	32	2.7

4.3 Data Acquisition

In the first set of experiments, phantoms were imaged on the Siemens Inveon™ micro-CT system. The standard x-ray source was set at a tube potential of 80 kVp, with an anode current at 500 μA. The large area indirect type FPD (4,096 × 4,096 pixel elements, 10 × 10 cm field of view) was binned by a factor of 4, resulting in effective detector element size of 122 μm. Each acquisition was a full 360° rotation of the detector-source assembly with 120 views or projection angles. The distance of center of rotation of source from the x-ray focal spot was set at 264.03 mm while the source to detector distance was set at 334.47 mm. All the acquisitions were performed with an added tube filtration of 0.5 mm Al equivalent. While imaging the phantoms, care was taken that their cylindrical portion projected out of the bed pallet to avoid beam attenuation due to bed material.

4.4 Data Reconstruction

Image reconstruction was performed using the standard Feldkamp algorithm for cone beam CT reconstruction, with a Shepp-Logan filter with cutoff at the system Nyquist frequency resulting in an image matrix of 256 × 256 × 256 with an isotropic voxel size of 0.386 mm. The cylindrical water phantom of diameter 28 mm can be used for HU scale factor determination for reconstruction of all CT images. For each phantom data, the reconstruction was done in two ways –

1. Without applying any BH correction.
2. By applying manufacturer's default BH correction values represented by a third order polynomial as:

$$f = a_0 + a_1 x + a_2 x^2 + a_3 x^3 \qquad (4.1)$$

The coefficients a_0, a_1, a_2 and a_3 are the actual correction factors in **Fig. 3.3**, which help linearize the attenuation measurements from the polyenergetic spectrum, towards the expected values of attenuation at a specific level of "effective energy". The significance and determination of this "effective energy" is described in Sec 5.3.1.

CHAPTER 5

METHODOLOGY

5.1 Design of Data Processing Workflow

The method of BH correction using linearization depends on knowledge of the composition and material density of the object being imaged. However, before this correction can be achieved, a function relating the object thickness to the polyenergetic CT data has to be carefully measured. This relationship is non-linear and also known as the *Beam Hardening Curve* for the material under consideration [shown in Fig 5.1].

The initial slope of this beam hardening curve is crucial to derive the final transformation equation from polyenergetic attenuation data to the ideal "effective" attenuation values. Hence, for each phantom type and material, the requisite beam-hardening curve is obtained as described below.
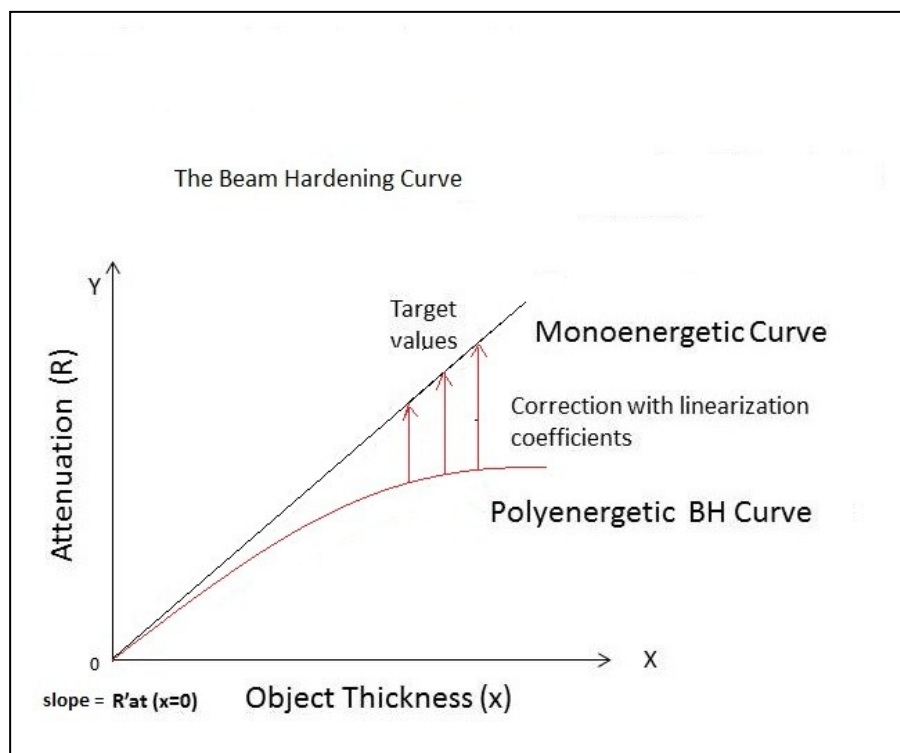
Figure 5.1 Schematic illustrating process of linearization of CT data

5.1.1 Data Normalization

Prior to every image acquisition, a pair of 'dark' and 'light' acquisitions is performed with an empty field of view. Multiple 'dark' projections are acquired first, with the x-ray source and anode current turned off. It represents the noise generated from the electronic dark current and sensitivity bias in the CCD detector system. Next, the 'light' exposure is obtained; the source is energized and a full exposure of the detector array is initiated at the anticipated energy and current settings to be used to scan the object. By averaging the multiple projections in each acquisition, 'dark' and 'light' *calibration* frames are obtained. These are symbolically represented as I_d and I_o respectively. The object is then placed in scan FOV and raw projection data (I_m) is acquired for each of the 120 views.

When generating a CT image of an object, a true measure of attenuation (R_{poly}) must be obtained from each measured projection frame. To get an accurate measurement it is critical to remove dark noise from the both the object and the light frame projection data through a dark frame subtraction from the measured projection frame *'I_m'* and the light calibration frame *'I_o' [Hammersberg et.al]*. The resultant light calibration frame is then used to normalize the resultant measured projection frame. This is depicted in the following equation:

$$R_{poly} = -\ln\left[\frac{I_m - I_d}{I_0 - I_d}\right] \qquad (5.1)$$
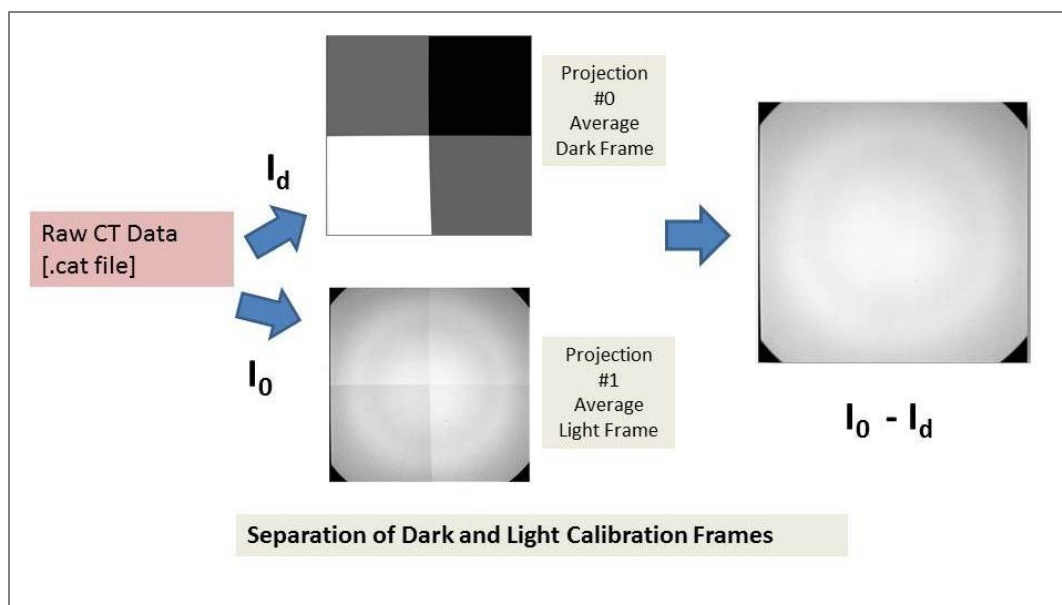
Figure 5.2 Shows dark and light calibration frames

The acquired CT raw data for each phantom is stored in the Inveon system in *.cat* format as 16-bit unsigned integer type with a pre-defined header block. As shown in the first step of the workflow, this raw data was used to extract the dark and light calibration frames (I_d and I_0) as well as actual projection data. **Fig 5.2** shows the necessary inputs given to the image processing toolbox in Fiji (ImageJ) for extraction of the required frames of data.

For each .cat dataset, eight different angles of projection data (of the 120 available) were selected for statistical accuracy in the subsequent stages of analysis. The discrete set N of 8 different projections angles (in degree) is represented as:

$$N = \{0, 15, 30, 45, 60, 75, 90, 105\}$$
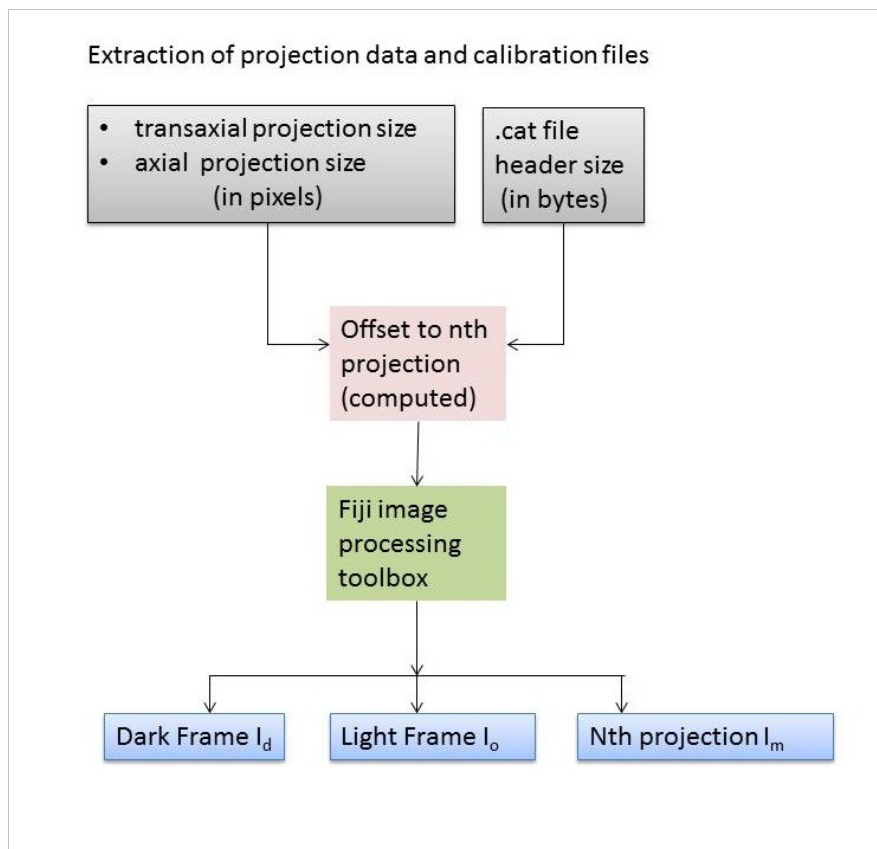
Figure 5.3 Sequence of derivation of actual intensity values from raw CT data. The steps are applied for each projection angle $n \, \varepsilon \quad N$
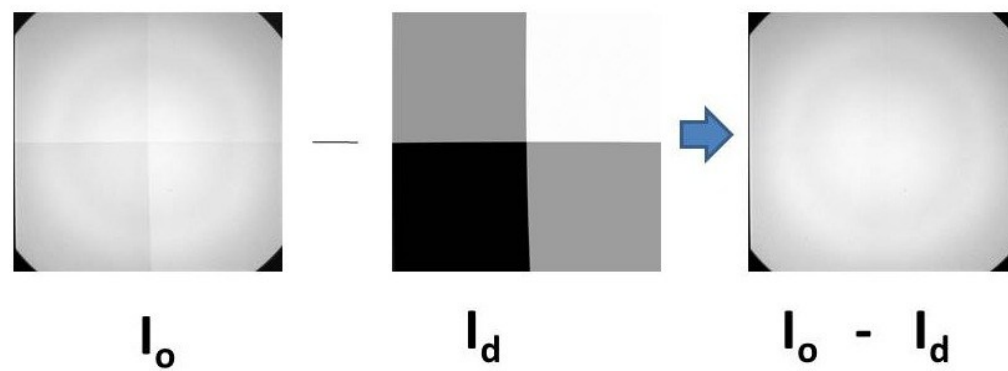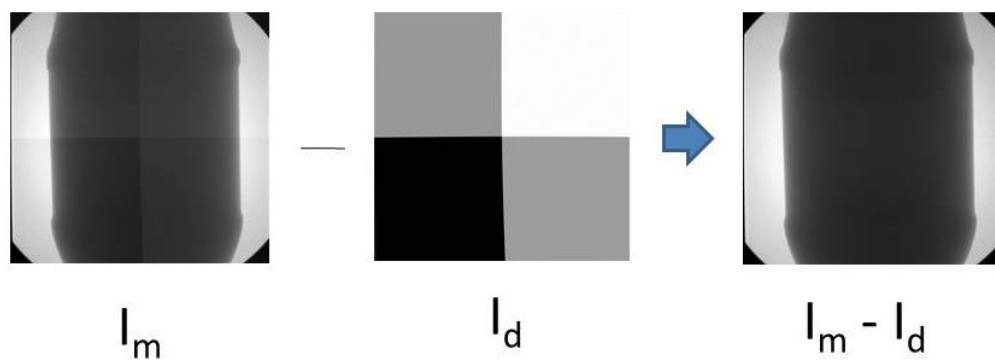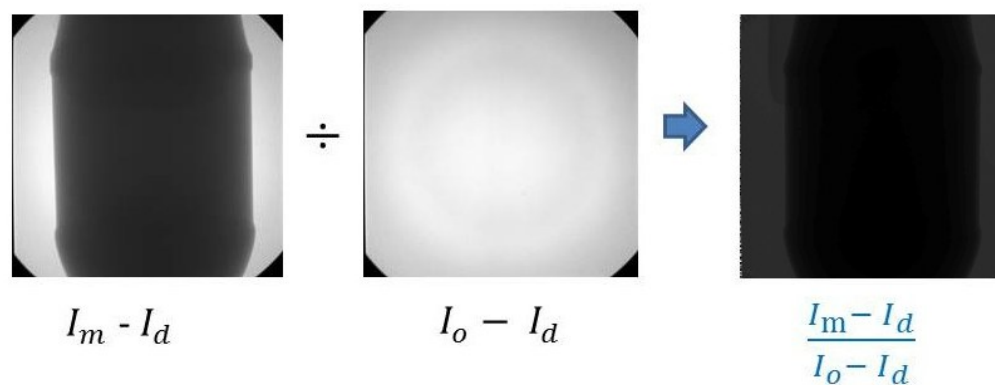
Figure 5.4 Steps of raw data preprocessing for derivation of true values of beam attenuation

After the extraction of dark and light calibration files, I_d is subtracted from I_0 resulting in an intensity map $[I_0-I_d]$. For each projection n ϵ N, the dark frame 'I_d' is also subtracted from the measured projection value 'I_m' each resulting in a 2D intensity map of $[I_m-I_d]$. All maps thus created have a size of 1024 rows and 992 columns. **[Fig 5.4].** The final phase of processing is to compute the ratio of intensity maps obtained in **Steps I** and **II**. The final **Step III** shows this ratio of intensity maps.

5.1.2 Analysis of Attenuation Map in Matlab

The ratio of intensity maps for each projection angle (n ϵ N) was imported into the Matlab environment. From each intensity map, the attenuation map was derived by taking its negative logarithm (as represented by **Eq 5.1**). Each such attenuation map was thus visualized as shown in **Fig. 5.4**, consisting of 1024 rows and 992 columns. Each column in this 2D matrix thus represents measurements by a single column of detector elements. Each matrix entry shown in Figure 5.4 contains the value of R_{poly} where,

$$R_{poly} = -\ln\left[\frac{I_m - I_d}{I_0 - I_d}\right] \qquad (5.2)$$

Therefore, for each entry in the R_{poly} matrix of attenuation map, we can calculate μ if we know x, the thickness of the attenuating material. In this work we calculate x based upon the geometry of the cylindrical phantom within the FOV. The methodology for determining chord lengths 'x' is discussed in Sec 5.2 below.

Attenuation values of 7 consecutive columns (#493- # 499) shown in Figure 5.5B were averaged to obtain the final values of attenuation for a given angle of projection. Selection of these columns was based on the fact that these slices lie in the center of the detector FOV and hence are functionally perpendicular to the axis of the cylindrical phantom. Therefore the x-ray paths through the phantom in these slices generate chords of a circle whose chord lengths are easily calculable. Six slices were chosen and averaged

to generate for higher statistical accuracy of attenuation values. The slices are thin enough (~386.5 μm) so that geometrical errors for calculation of chord length are << 1%.

$$R_{poly} = - \ln \left[\frac{I_m - I_d}{I_o - I_d} \right]$$
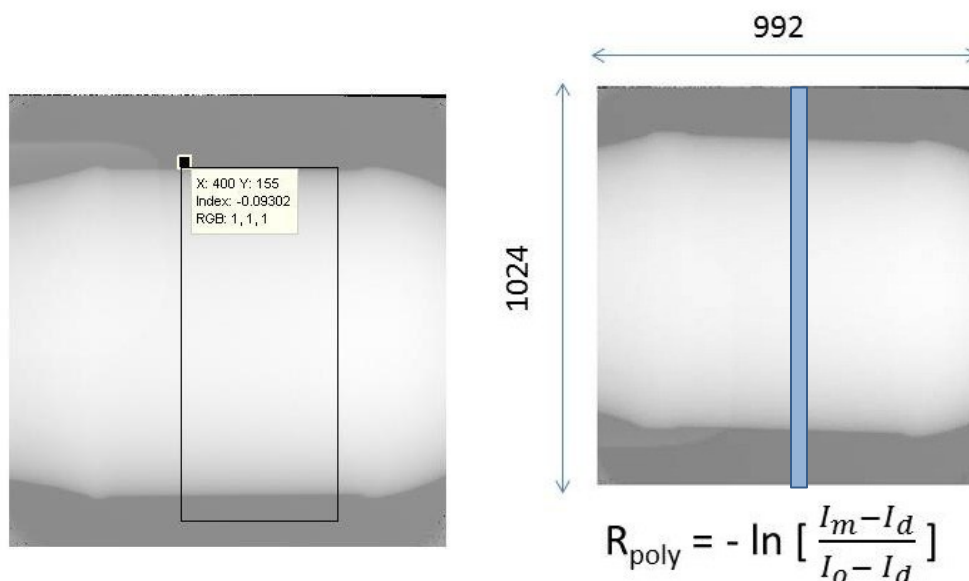
Figure 5.5 Left -Shows region of the 2D attenuation map (column# > 400) suitable for analysis, as it avoids attenuation due to the portion of bed pallet supporting the cylinder. **Right -** Attenuation map for a single projection. For each view, the values of attenuation between the columns 493 – 499, indicated by blue bounded region, were averaged.

5.2 Length of X-Ray Propagation through Material

5.2.1 Location of Object Center w.r.t Geometric Isocenter

The center O' (x',y') of the scanned object does not necessarily coincide with geometric isocenter of the scanner O as shown in Fig. 5.5. This difference or offset has an effect on the calculation of x-ray path lengths through the object. Hence the offset between object center and scanner isocenter was determined. To measure the offset, the raw CT data for each phantom was reconstructed with the Inveon CT reconstruction protocol. No beam hardening correction was applied during reconstruction. A 256 x 256 slice of midway along the axial extent of the scanned object was reconstructed. A

threshold was applied to delineate the object boundaries from the background. From this delineated shape, the object center coordinates O' (x',y') was determined. Offset between O(x,y) and O'(x',y') denoted by 'dx' and 'dy' respectively was calculated as:

$$dx = |x' - x| * \text{reconstructed pixel size in mm}$$
$$dy = |y' - y| * \text{reconstructed pixel size in mm}$$
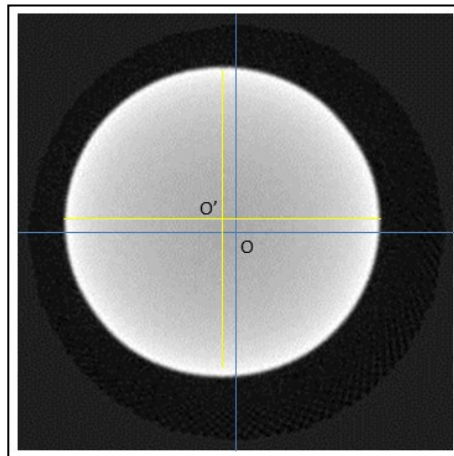
Figure 5.6 Reconstructed image on axial plane visualized on ImageJ shows spatial difference between geometric isocenter (O) of the scan field of view and the center of object (O').
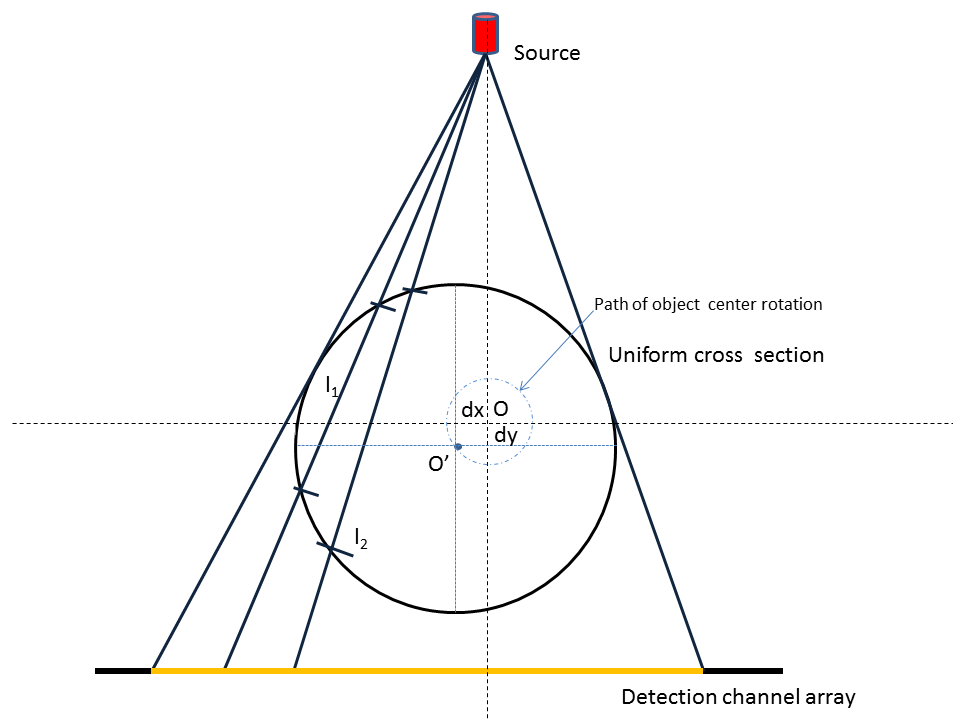
Figure 5.7 Uniform cross section of object showing the difference between center of object O' and geometrical isocenter O. Assuming stationary source, the object center O' rotates around O with a fixed radius OO' = $\sqrt{(dx^2 + dy^2)}$

While the distance between O and O' remains constant, the coordinates (dx, dy) vary, with change in position of rotating source (projection angle) around the stationary object. This is illustrated in **Fig. 5.6** where the coordinates (dx, dy) of the center of object follow a circular path around the geometric isocenter 'O'. A custom MATLAB function was scripted to determine the coordinates (dx, dy) for each projection angle (n ϵ N).

5.2.2   Algorithm For Length of Propagation

As shown in Fig. 5.6 the x-ray photons emanating from the focal spot of the source undergo attenuation while passing through the medium. This distance is calculated using a second custom MATLAB function whose inputs are the coordinates (dx, dy) of object center O' calculated in the previous section. Other inputs to the function are:

- ▪ Radius of the object
- ▪ Distance of source from center of rotation, O. (Fig. 5.7)
- ▪ Distance of detector array from center of rotation O.
- ▪ Detector pitch in mm

The output of the function is a one dimensional array L(r) of lengths of x-ray paths through the medium, the largest calculated path-length being equal to the diameter of the uniform cylindrical phantom passing through O'.
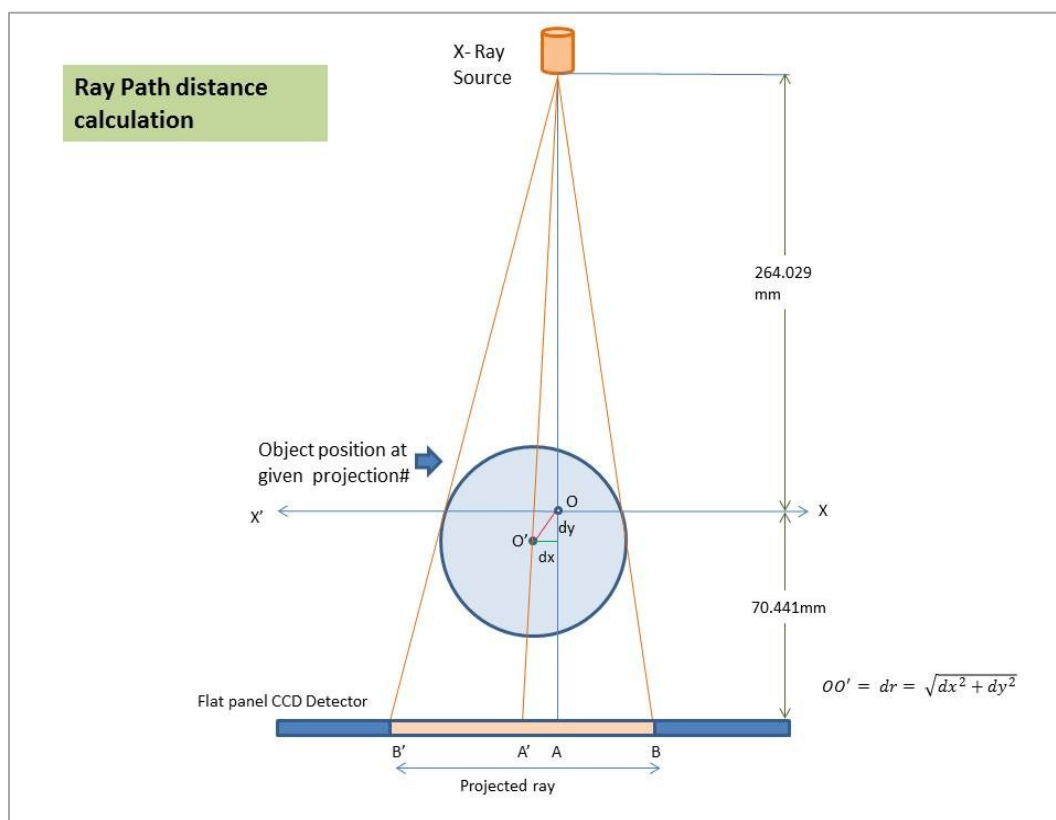
Figure 5.8 Overview of scanning geometry - O (0, 0) = geometric isocenter of scanner taken as origin, O' (dx,dy) = center of uniform axial cross section of object being imaged, BB' = projected cone beam ray on the detector.

5.3 Polynomial fitting of Polyenergetic BH Curve

As mentioned earlier in Sec. 5.1, the non-linear curve describing the relationship between attenuation and object thickness is necessary to determine the final correction factors which transform the polyenergetic data to expected or ideal values of attenuation. This has been represented schematically in Fig 5.1. The curve is first fitted with a polynomial of third degree. The slope or gradient of this fitted BH curve at zero object thickness (x=0) is used to determine the ideal curve which represents values of attenuation that would be obtained in case of a monoenergetic source spectrum of the effective energy $\overline{E}$. *[Hammersberg et.al]*

5.3.1 Estimation of Effective Energy of unknown X-ray spectrum
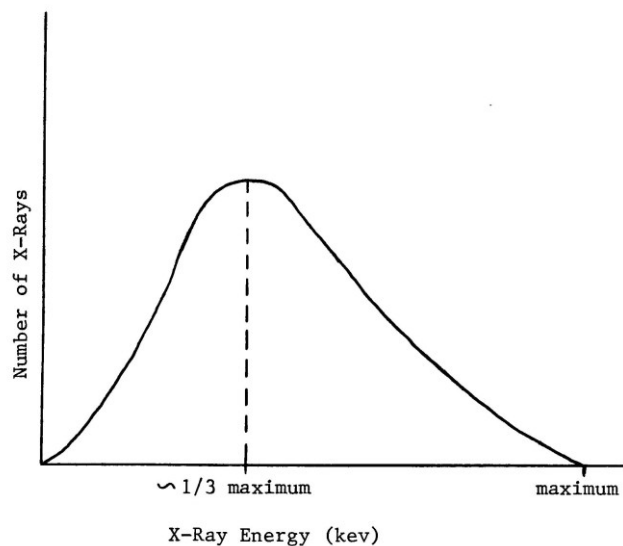
Figure 5.9 Effective energy of a continuous x-ray spectrum [25]

The **effective energy** of an x-ray spectrum is defined as the energy of a mono-energetic beam of photons that has exactly the same penetrating ability as the incident spectrum of photons. Typically, the Half-Value-Layer (HVL) is the most frequently used quantity for describing the penetrating ability of x-ray spectra through a specific material. HVL is defined as the thickness of material required to attenuate the intensity of incident radiation by one half. For a given HVL for an incident spectrum and a specific attenuating material, there is a corresponding monoenergetic photon energy that shares that HVL. This photon energy is the **effective energy** of the spectra, and this value plays a critical role in the linearization correction method to be discussed. Typically the effective energy is about 30%-40% of the maximum photon energy, but its exact value depends on the shape of the spectrum.

The slope of the BH curve at near-zero object thickness (as shown in **Fig 5.1** corresponds to the *effective linear attenuation coefficient* where $\overline{E}$ represents the *effective energy* of the unknown x-ray spectrum. Therefore a single effective energy can be used to represent the monochromatic projection for the entire polychromatic spectrum.

$$\left. \frac{d\left(R_{poly}\right)}{dx} \right|_{(x=0)} = \mu\left(\overline{E}\right) \tag{5.3}$$

5.3.2   Generation of Expected Projection Data

As discussed in the previous section, the initial slope of the beam hardening curve determines the value of $\mu(\overline{E})$. This value is used to estimate the expected values that correspond to the ideal values of attenuation if the spectrum were a monoenergetic beam of photons of energy $\overline{E}$. Hence, each element of the one-dimensional array of object

thicknesses L(r) [Refer Sec. 5.2.2] is multiplied with the value of $\mu(\overline{E})$ to obtain the expected or corrected values of projection as below:

$$P_{corrected} = \mu(\overline{E})x \tag{5.4}$$

5.4 Linearization of Polyenergetic Data

In the final step of the proposed correction scheme, a mapping function f is derived from the original polyenergetic projection data to the computed monoenergetic projection from Sec 5.3.2.

$$P_{corrected} = f(P_{measured}) \tag{5.5}$$

This function 'f' is a polynomial of third degree represented as:

$$f = a_0 + a_1 x + a_2 x^2 + a_3 x^3 \tag{5.6}$$

The above calibration coefficients [a_0, a_1, a_2, a_3] of this third degree polynomial were used as inputs to the BH correction model built into the CT reconstruction protocol on the Inveon system. The method was tested and validated using phantoms of different sizes and materials. Reconstructed images were compared with the reconstructed images when 'default' values of beam hardening correction was applied.

CHAPTER 6

DATA ANALYSIS AND REPRESENTATION

This project had two general aims. First and foremost it was our intent to characterize and correct for beam hardening in the Inveon CT system for a variety of acquisition settings (12 different kVp and filtration combinations were characterized) using water as the medium. This aim was particularly important because water is the preferred surrogate material for purposes of beam hardening correction for mouse and rat imaging (as well as human). The second aim was to generate beam-hardening corrections for several materials other than water. This work was done only at a single kVp and filtration setting.

In the following sections, we illustrate the basic characteristics of the beam hardening curve obtained from the raw projection data for each phantom under consideration. For each phantom type and size, the chart shows the relationship between measured values of attenuation due to the polyenergetic spectrum, mapped against the calculated distance of propagation of x-ray through the object. Using these characteristic curves the BH correction function was generated.

6.1 Uniform Water Cylinder [Ø =71 mm]
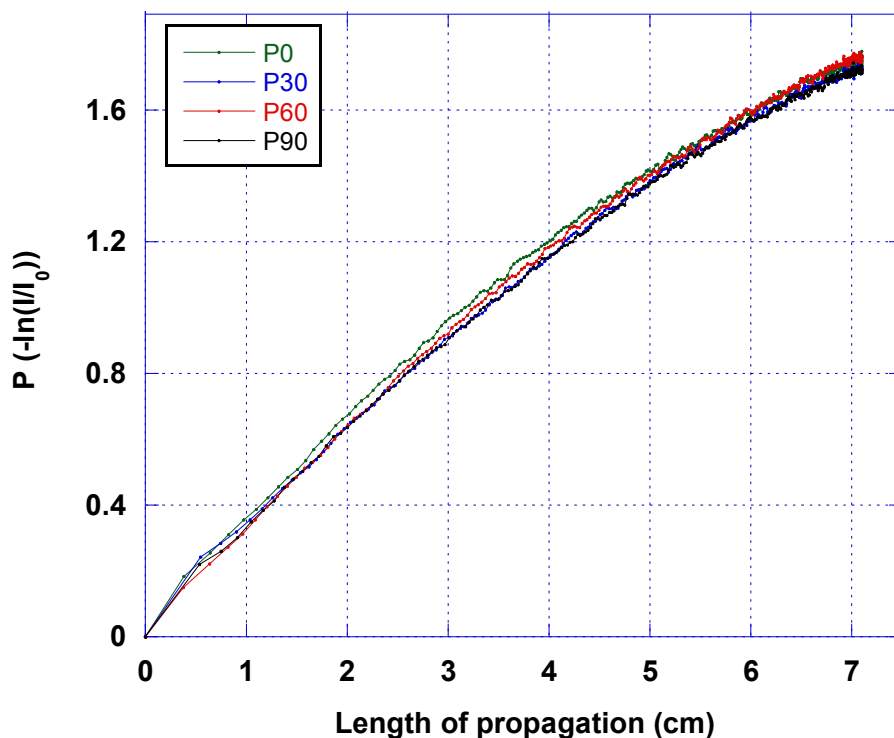
Figure 6.1 Beam hardening characteristic curves for uniform cylindrical water-filled phantom (Ø =71 mm) sampled for a set of four projection angles – 0º, 30º, 60º and 90º [At acquisition settings: 80 kVp , 0.5 mm added aluminum filtration]

From a given BH curve, the final correction function can be estimated by first determining the initial slope of the curve [**Sec.5.3**]. Prior studies have indicated that in order to generate a calibration or correction function for beam hardening, the initial part of the BH curve is critical since it defines the $\mu_{eff.}$ (since at smaller x-ray path lengths, the effect of beam hardening can be largely neglected) [24]. As an example, we show in **Fig.6.2** the BH characteristic curve for attenuation measurements taken at projection angle - 15º of a scan of a water phantom acquired with peak voltage of 80 kVp.

Fig. 6.2 shows the third order polynomial fit to the curve. It is important to note that in Figures 6.1-6.2 that we are analyzing a single kVp/filtration combination, and that similar measurements and calculations were performed on 11 different commonly used kVp filtration combinations.
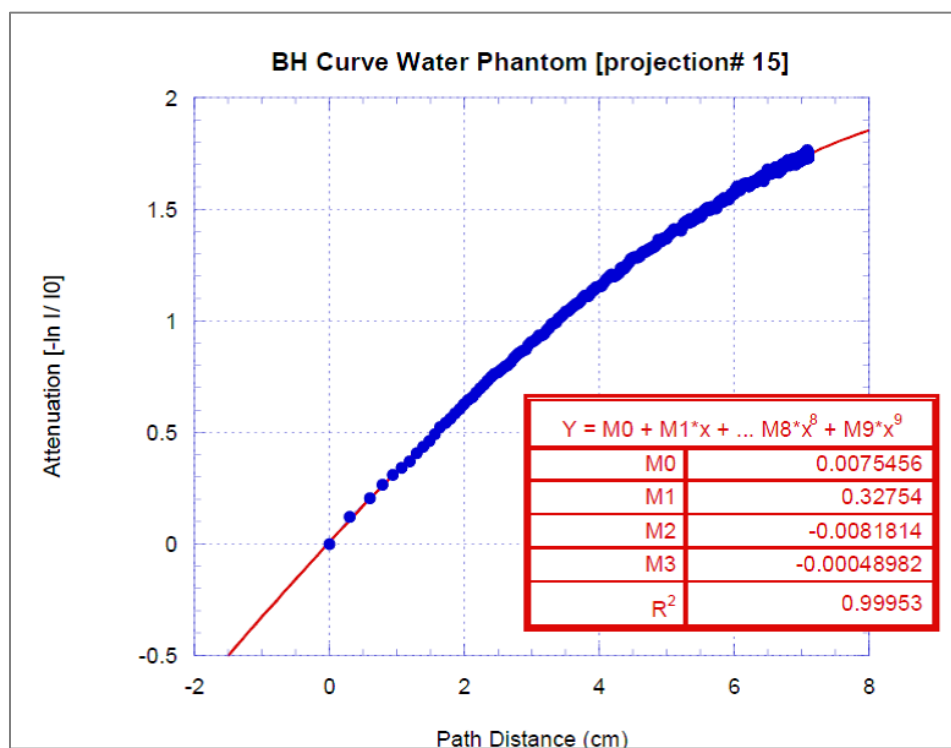
Figure 6.2 BH curve fitted to polynomial of third order for 71 mm diameter water-filled phantom.

From Fig 6.3, the value of coefficient 'M1' represents the slope or gradient of this fitted BH curve at zero object thickness (x=0).

This value of slope is used to determine the ideal curve that represents values of attenuation that would be obtained in case of a monoenergetic photon beam whose energy is equal to the effective energy, E_{eff}, of the present spectrum. [Section 5.3.1.]

The range of values of the initial gradient of the BH curve for different sampled projection angles was observed to be between 0.434-0.4297. According to the NIST standard reference database for x-ray attenuation of water [23], this range of $\mu(\bar{E})$ corresponds to the effective energy range between 26 keV to 28 keV.

Generation of third order correction polynomial - Using the value of slope M1 from Eq. 6.1, the correction function is estimated as shown in **Fig 6.3**. The attenuation expected for equivalent monoenergetic beam energy is represented as '$P_{corrected}$' while the original polyenergetic attenuation is represented as '$P_{measured}$'. Sec 5.4 describes the process of generation of the third order polynomial for BH correction in detail.

The correction function has to be a polynomial of third degree in order to be compatible with the built-in correction mechanism of the Inveon μCT system. The coefficients thus obtained are shown in Table 6.1. These coefficients are then applied as a preprocessing step for BH correction of original raw CT data and the corrected projection data are then reconstructed to obtain the final images. The above analysis was repeated for other phantom materials as illustrated in the following section.
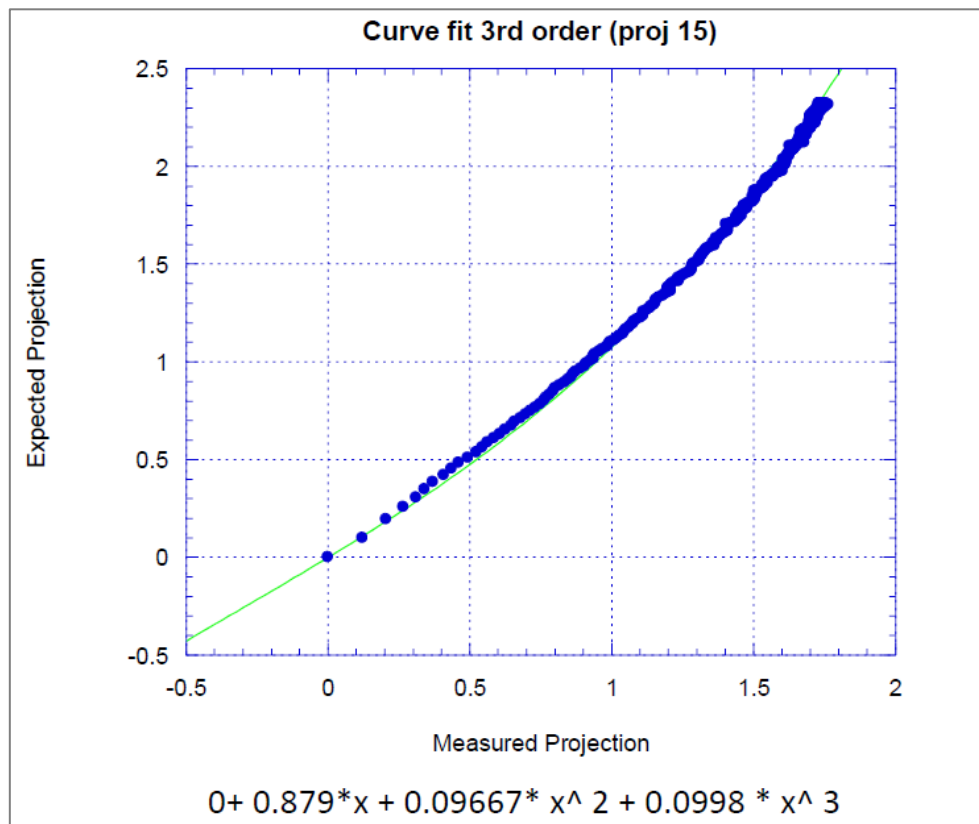
Figure 6.3 Generation of final mapping function for BH correction.

Table 6.1 BH correction coefficients for water used during final image reconstruction

Coefficient	Value
a0	0
a1	0.879
a2	0.09667
a3	0.0998

6.2 Low Density Polyethylene (LDPE)

$\rho \sim 0.94 - 0.97$ g/cc
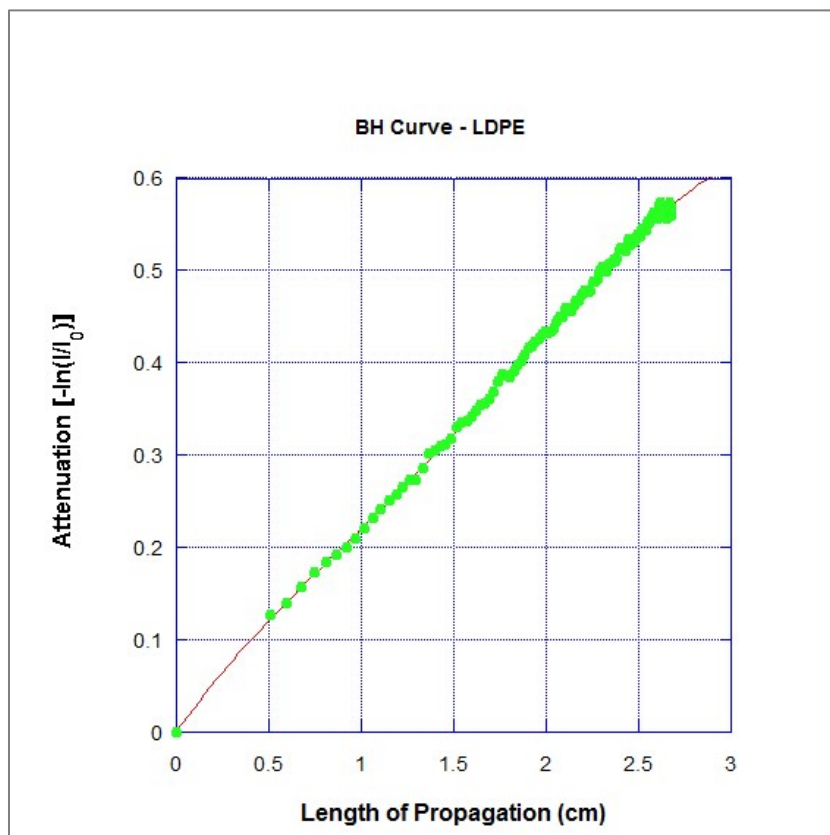
Figure 6.4 Beam hardening characteristic curve fitted with fourth order polynomial for Polyethylene. As observed, gradient of curve at (x=0) is equal to 0.285 which corresponds to energy ~ 28 keV.

Table 6.2 Coefficients of polynomial fit for BH curve for LDPE

M0	0.00080148
M1	0.28555
M2	-0.11931
M3	0.065508
M4	-0.011619
R^2	0.99893
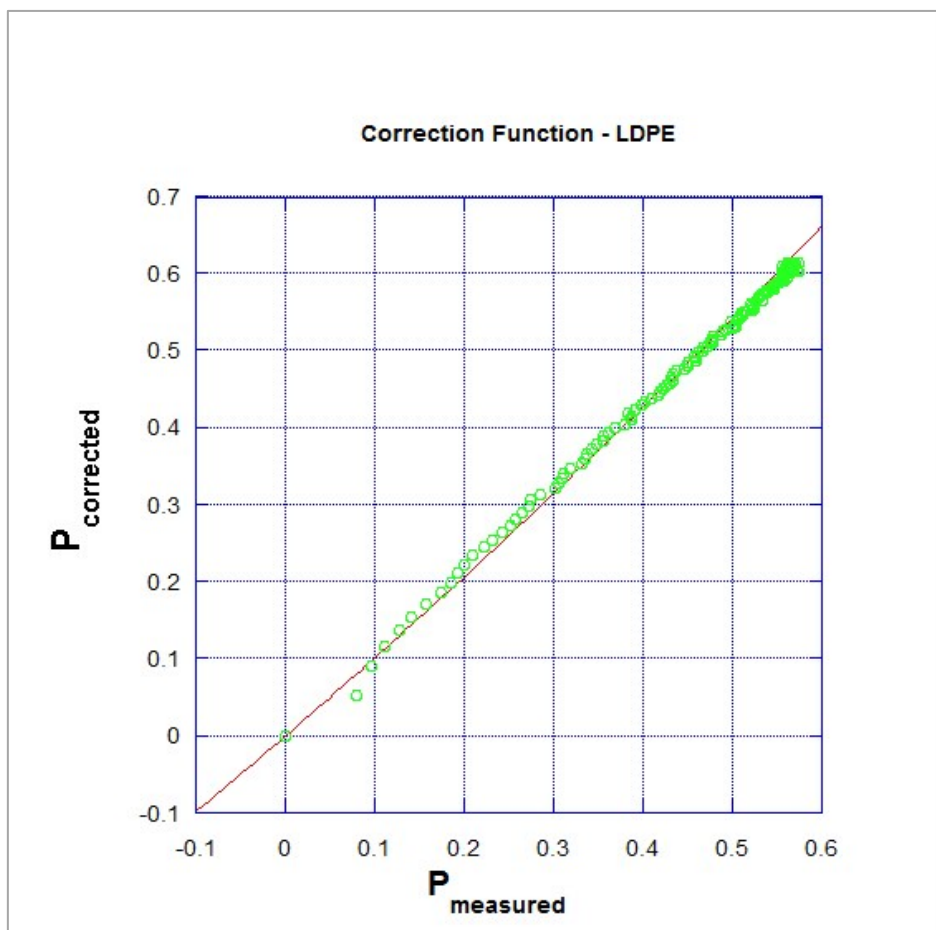
Figure 6.5 Generation of final mapping function for BH correction**.**

Table 6.3 BH correction coefficients for LDPE

Coefficient	Value
a0	0
a1	0.9987
a2	0.166
a3	0.01

6.3 Delrin/ Polyoxymethylene $(CH_2O)_n$
$\rho = 1.411$ g/cm^3
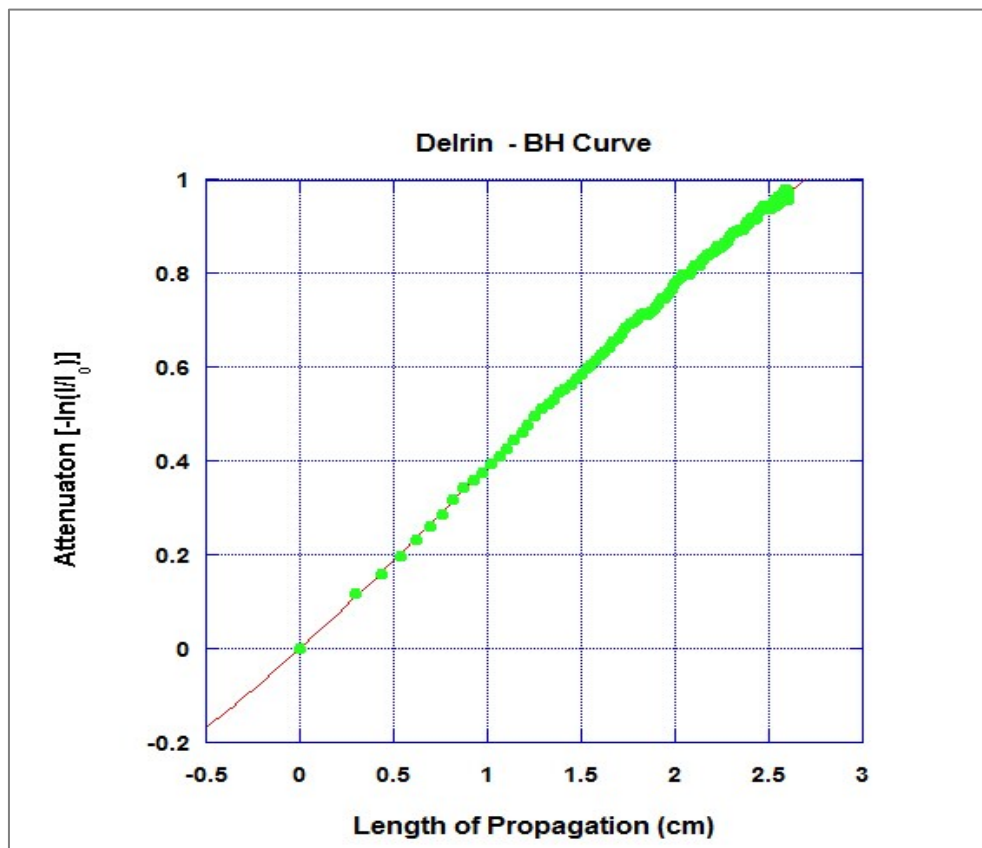
Figure 6.6 Beam hardening curve fitted with third degree polynomial for Delrin (polyoxymethylene). As observed, gradient of curve at (x=0) is equal to 0.36, which is used to generate final correction function.

Table 6.4 Coefficients of polynomial fit for BH curve for Delrin

Rpoly = M0 + M1*x + M2*x^2+M3*x^3	
M0	0.00023556
M1	0.36059
M2	0.042008
M3	-0.014196
R^2	0.9995
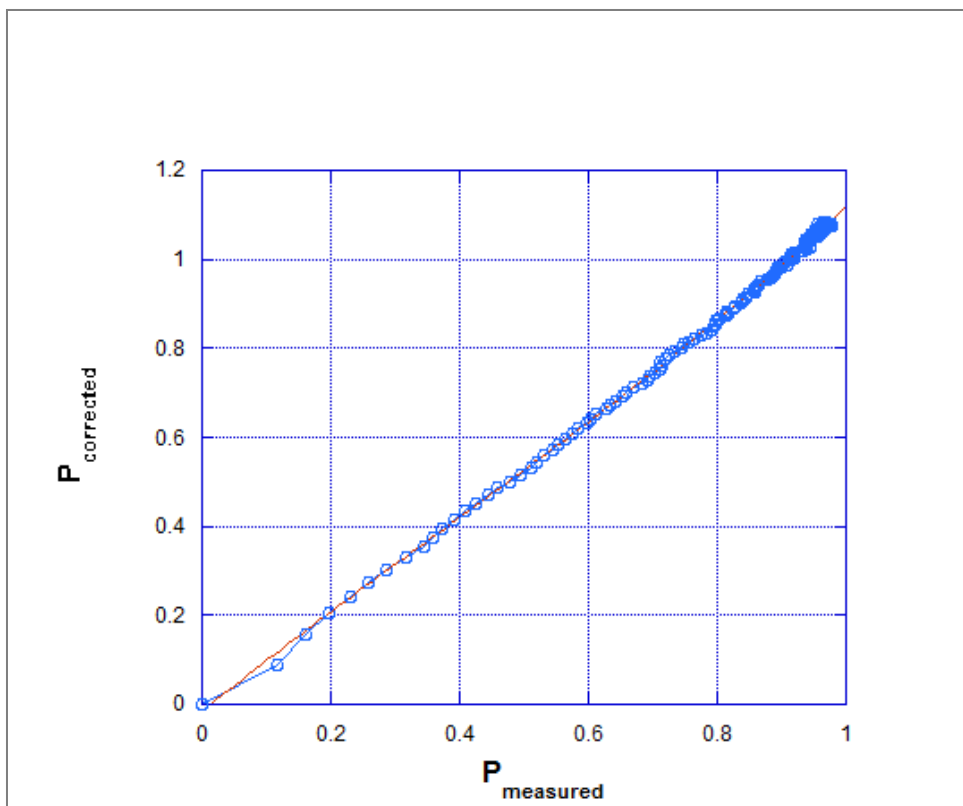
Figure 6.7 Correction function generated for Delrin**.**

Table 6.5 BH correction coefficients for Delrin

Coefficient	Value
a0	0
a1	0.945
a2	-0.169
a3	0.193

6.4 Aluminum

$(\rho = 2.7 \ \text{g/cc})$
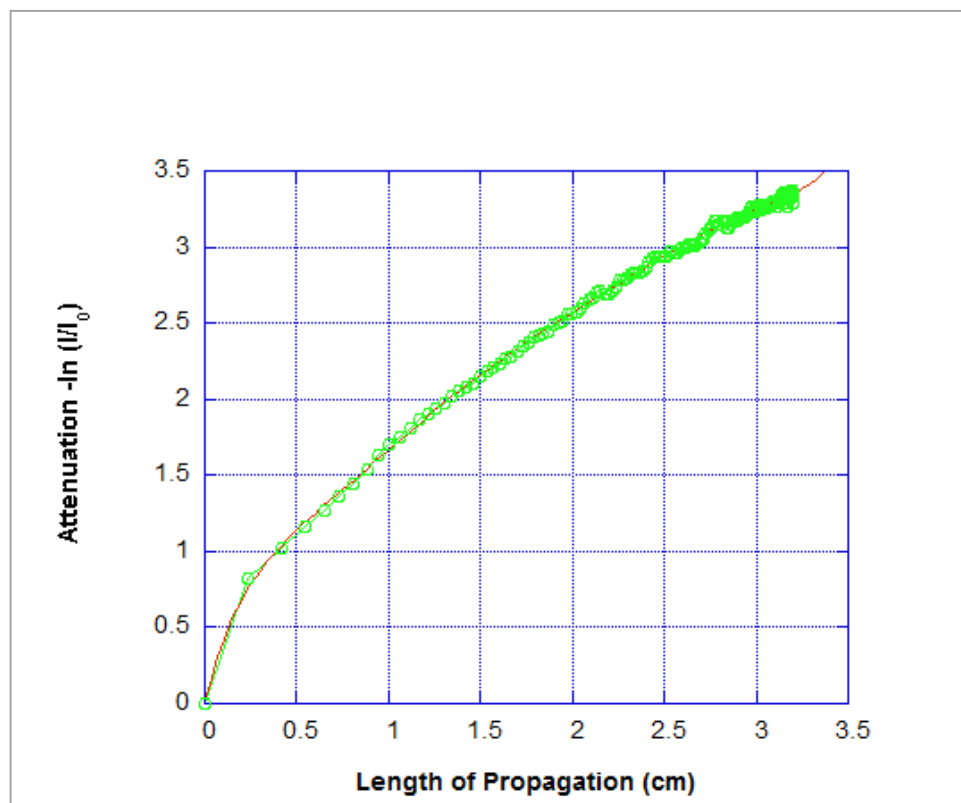
R poly = M0 + M1*x + ... M8*x^8+ M9*x^9	
M0	0.018207
M1	4.5958
M2	-8.3483
M3	10.128
M4	-6.8232
M5	2.5522
M6	-0.4968
M7	0.039213
R^2	0.99871

Figure 6.8 Beam hardening characteristic curve fitted with 7th order polynomial for Aluminum. As observed, gradient of curve function at (x=0) is equal to 4.5958, which corresponds to effective energy value of approximately ~ 26 keV.
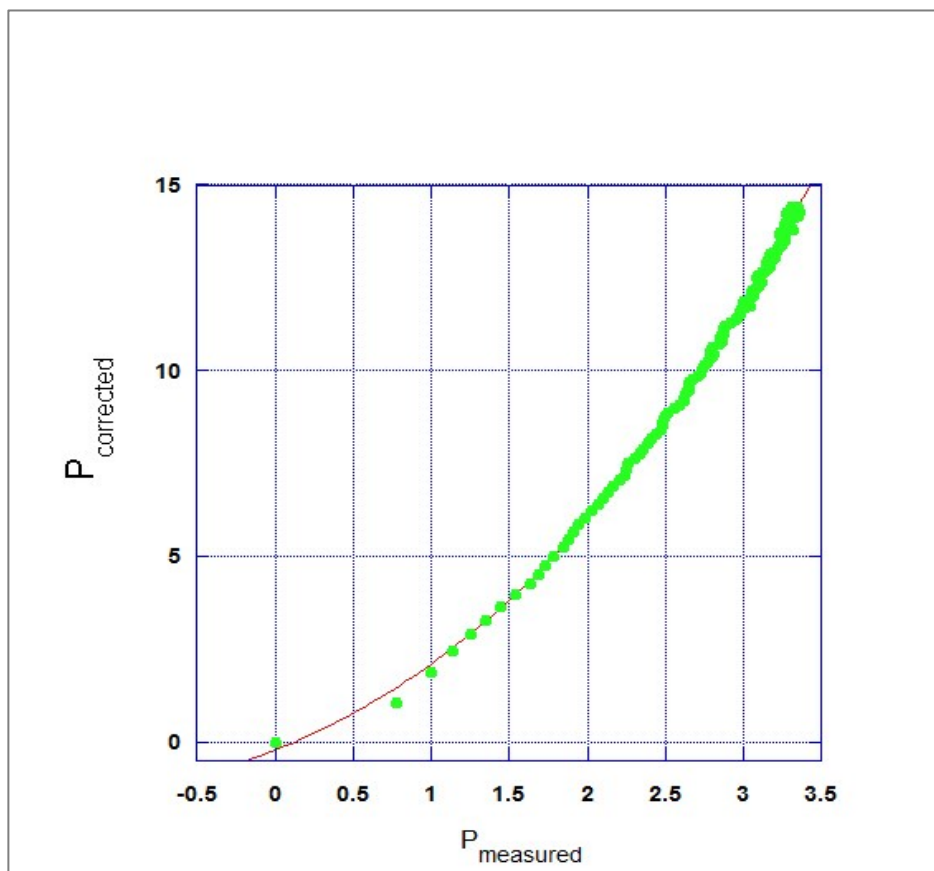
Pcorrected = a0+a1*x+a2*x^2+a3*x^3	
a0	-0.2164
a1	1.6637
a2	0.58674
a3	0.065069
R^2	0.99811

Figure 6.9 Generated mapping function for BH correction for Aluminum

CHAPTER 7

RESULTS

As we have seen previously, the current beam hardening correction implementation on the Inveon CT system is inadequate to accurately perform quantitative reconstructions, particularly on larger objects. It was the primary purpose of this project to characterize beam hardening at several peak voltages and with different filtrations for water. This is critical information because it is these corrections that will be applied to standard animal image data. It was a secondary aim of the project to develop beam-hardening corrections for other materials besides water.

For each of the cylindrical phantoms imaged, the mapping function generated for each phantom material (including the water experiments) was used to correct the respective polyenergetic projection data. The corrected projection data was subsequently reconstructed to obtain the final beam-hardening corrected images. For the sake of comparison, each phantom data was reconstructed in three different ways:

- without application of BH correction
- with application of 'default coefficients' built-into the Inveon system.
- with application of newly generated mapping/correction function.

Since all the reconstructed images are scaled to standardized Hounsfield Units (HU), any modification in BH correction settings also affects the scanner's calibration of image scale factor to HU. Hence, prior to using any newly generated coefficients for BH correction of phantom data, the necessary scale factor for calibration of CT data to Hounsfield Units was determined. This calibration is done by imaging a 50 ml centrifuge tube filled with water using the standard calibration methods defined for the Inveon system. The following sections illustrate the reconstructed images and the corresponding axial profile diagrams for all three cases considered for reconstruction.

A) Uniform Cylindrical Water Phantom

Figure 7.1 Axial profiles of reconstructed images for 71 mm water cylinder. A) Top row - cupping artifact when no BHC is applied B) Second row - when default coefficients are applied C) Third row - when new coefficients are applied.

From Fig 7.1, it can be observed that the cupping artifact is significantly reduced for images, corrected using new set BHC coefficients derived from the correction scheme under study. For a rat-sized equivalent phantom, the new set of coefficients is more effective in reduction of cupping artifact, as compared to the default set of coefficients.

B) Low Density Polyethylene (LDPE)

Fig 7.2 shows the axial profiles of 26.7 mm polyethylene phantom. In case of polyethylene, when no BHC is applied, only a slight 'cupping' is visible. This is because of the small size of the object as well as its low density (~0.91 g/cc). However it is observed that application of default BHC coefficients, leads to over correction in the central region of the uniform phantom and a significant drop at the edges of the phantom, while this effect is better suppressed when new material-specific correction coefficients are applied.

C) Delrin/ Polyoxymethylene (POM)

Fig 7.3 shows the axial profiles for 26 mm diameter Delrin phantom. This material has a slightly higher density than water and LDPE. Hence when no BHC is applied, the cupping artifact is more prominent than observed in the case of LDPE. Similar to the case of LDPE, a significant drop around the edges is observed for ~ 5 mm when correction is applied with default coefficients. This effect is well suppressed when new coefficients for BH correction are applied, as the profile is observed to be flat throughout.

D) Aluminum

As observed in the case of Aluminum, the poly-energetic data has to be fitted with polynomial of 7th degree. The generally used procedure to fit a polynomial of second or third degree (as in case of less dense materials such as water, LDPE and Delrin) cannot be employed for Al [4]. The value of initial slope or gradient for BH curve for Al, (M1 =

4.4958) is much greater than 1 and hence the final correction polynomial generated by M1 has a linear coefficient value which is also greater than 1.

Since the highest value of correction coefficient allowed to be entered into Inveon's BH correction protocol cannot exceed 1, it is not possible to correct for BH in case of aluminum phantom using the derived coefficients.
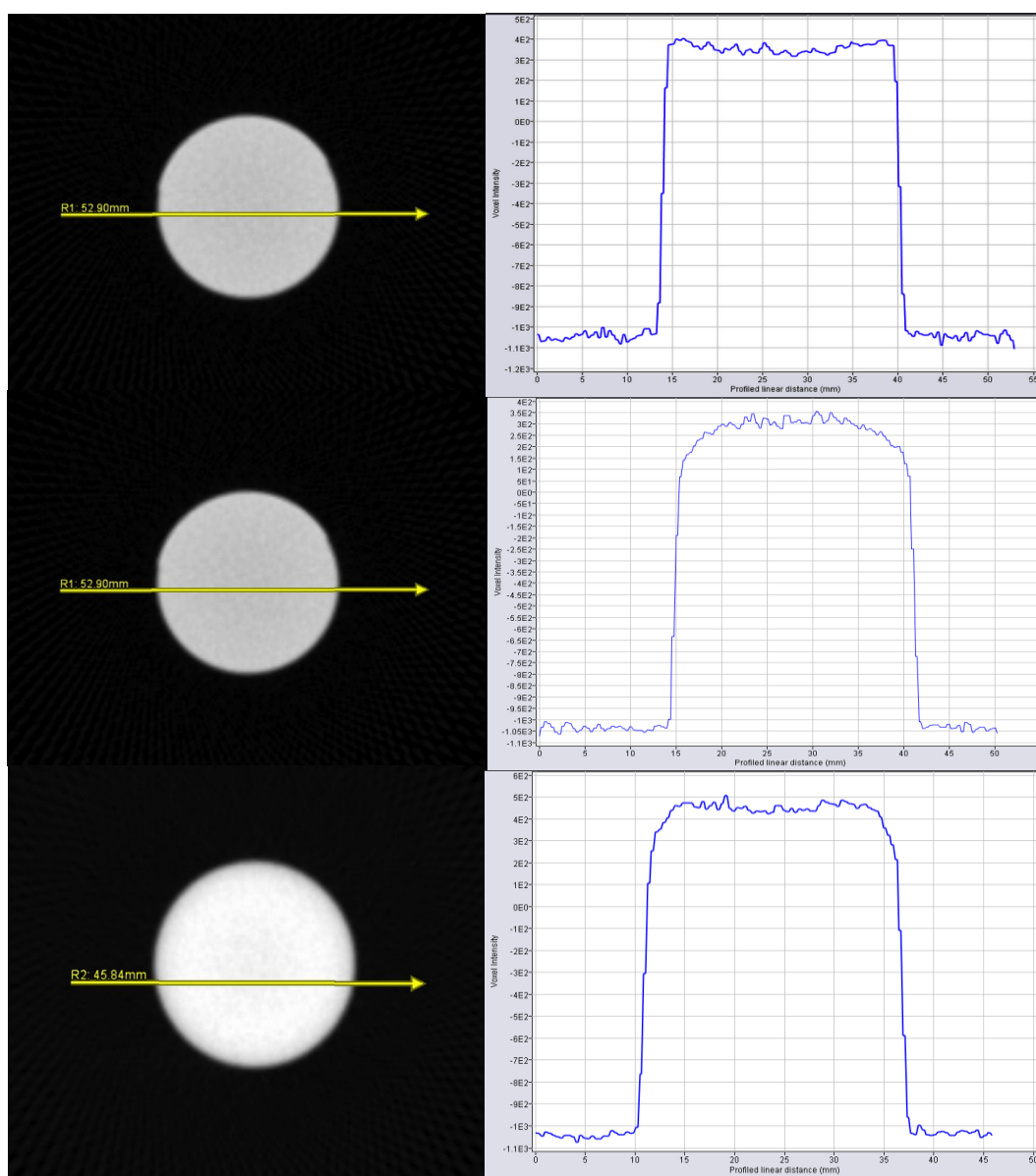
Figure 7.2 Axial profiles of reconstructed images for Polyethylene (LDPE). A) Top row - cupping artifact when no BHC is applied B) Second row - when default coefficients are applied C) Third row - when new coefficients are applied.
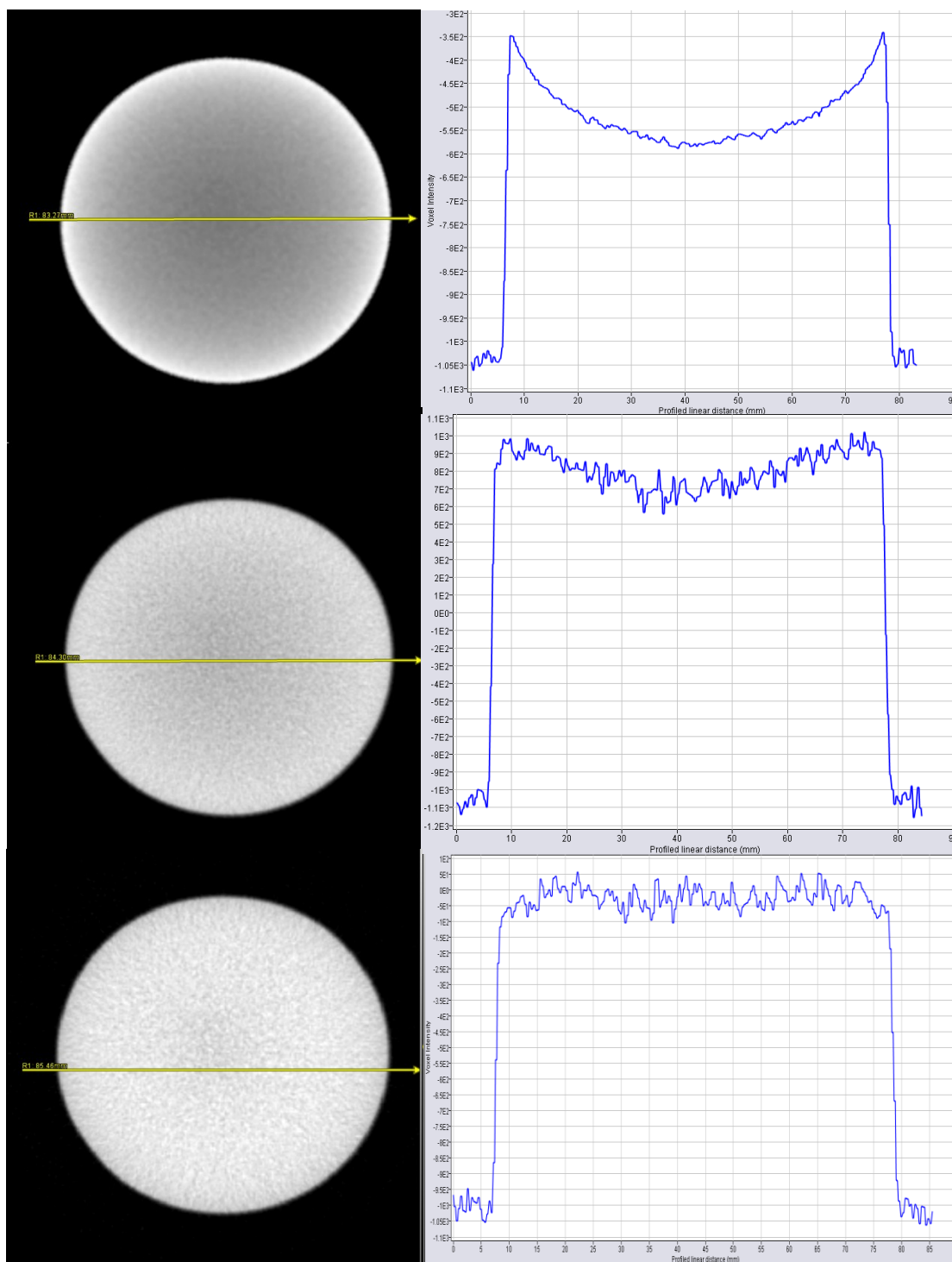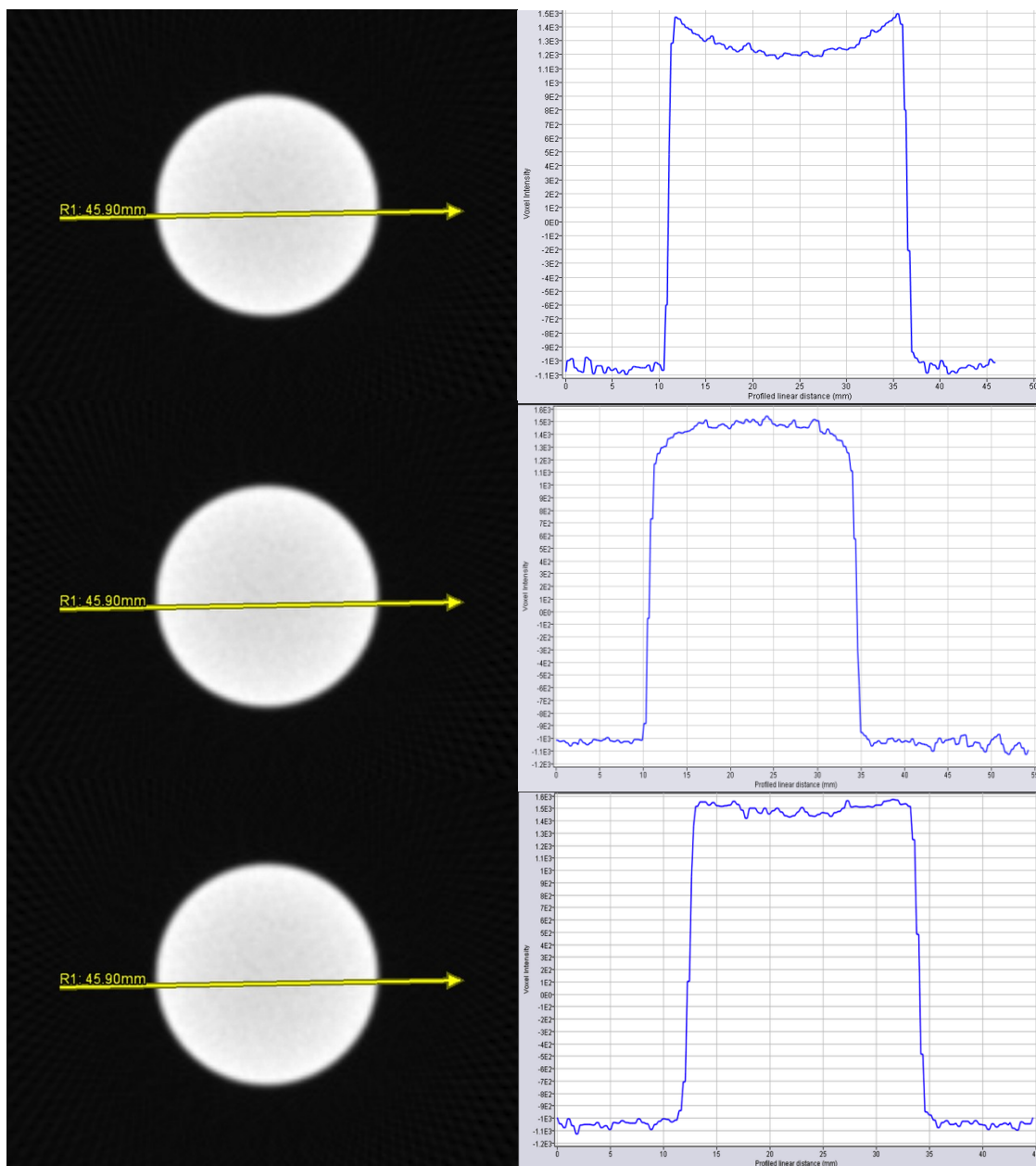
Figure 7.3 Axial profiles of reconstructed images for Delrin (POM) phantom. A) Top row - cupping   artifact when no BHC is applied B) Second row - when default coefficients are applied C) Third row - when new coefficients are applied.

7.1 Performance Evaluation w.r.t Improvement in CT Line Profile

For each material under consideration, we evaluated the extent of correction achieved with the generated correction coefficients, as compared to the respective uncorrected CT image. For each reconstructed sample, CT profile line diagrams were considered across the central region. For each sample, approximately 20 slices, at an interval of 5 were considered for in the middle portion of each cylindrical phantom. For each constructed profile the base of profile was scaled to 'zero' and the maximum gray value in the outer edge of each CT profile was scaled to '100'. The mean and SD of percentage enhancement of CT values in the central region with reference to base of the profile is evaluated for each sample. **Table 7.1** demonstrates a definite enhancement and improvement of CT profile in the central region of each sample.

Specifically for water phantom of rat size equivalent diameter, the 'uncorrected' case was considered with reconstruction using default coefficient values. From the analysis results, we can compare the performances of default coefficients and new coefficients for water phantom of 71 mm size. As compared to default coefficients, which result in an increment of 85.4% relative to the profile baseline, we can observe an enhancement of 94.3% in CT values using newly generated coefficients.

Since the default coefficients are functionally designed by Inveon for water and soft-tissue correction only, the 'uncorrected' case in solid phantoms was derived using reconstructions with no BH correction. However, in case of solid phantoms, it can be seen that the edge of the CT profile is better preserved as compared to the 'default' case. This is due to the fact that the solid phantoms are corrected with new coefficients which are derived from the actual effective linear attenuation coefficient for each solid phantom at the given spectrum energy.

Table 7.1 Percentage improvement of flatness of CT profiles after BH correction with generated correction coefficients.

Material	Phantom Diameter (mm)	Uncorrected		Correction With New Coefficients	
		% Mean	%SD	% Mean	%SD
Water	71	0.854	0.022	0.943	0.020
Delrin (POM)	26	0.894	0.004	0.941	0.006
Polyethylene (PE)	26.7	0.954	0.014	0.961	0.0219

7.2 Drop in CT Profile Edge After BH Correction

From the CT reconstructed profiles of water and other materials , it can be observed that a definite 'drop' towards the outer edge of the profile exists, starting from about 3/4th of the radius of the phantom from center. However, this inclination is not observed, when no BH correction is applied during reconstruction. This drop in edge has been studied and verified by Hammersberg et al. (1998). As a consequence of applying BH correction coeffcients and attempting to linearize the CT projection, the reconstruction sharpness (filtering and backprojection) is also altered which directly affects the quantitative measures of CT values in the final reconstructed image. MTF of the reconstruction algorithm is one of the several other factors (including detector width, focal spot size, geometric magnification, sampling density), contributing towards the total measure of modulation transfer function (MTF)of the imaging system [5] [29].

7.3 BH Correction Coefficients for Different Acquisition Conditions

It was found during the study that the correction coefficients that are generated for each material of phantom, are specific to a particular energy spectrum (80 kVp, at 0.5 mm added filtration). The proposed correction technique was also used to generate

coefficients for four specific and commonly used peak anode voltages - **40, 50, 60 and 80 kVp**. At each peak voltage level, the spectrum was modified with **0.5 mm, 1.0 mm and 1.5 mm Al equivalent** tube filtration in addition to the inherent 0.5 mm Al tube filtration.

In this way, we obtain 12 distinct sets of correction coefficients, therefore substantially expanding upon the quantitative performance of the Inveon μCT system.

Table 7.2 Values of correction coefficients estimated for water phantom of diameter 71 mm, corresponding for 12 combinations of kVp-filtration.

Peak Anode Voltage (kVp)	Additional thickness of tube filtration (mm)								
	0.5			1			1.5		
$a_0 = 0$ for all	a1	a2	a3	a1	a2	a3	a1	a2	a3
40	0.991	0.063	0.036	0.985	0.517	0.005	0.980	0.126	0.063
50	0.973	0.225	0.033	0.991	0.137	0.084	0.968	0.127	0.083
60	0.944	0.127	0.048	0.945	0.193	0.050	0.949	0.102	0.091
80	0.879	0.097	0.099	0.989	0.278	0.194	0.952	0.234	0.055

CHAPTER 8

DISCUSSION

Significance of Study

This research has broadened our understanding of the physical processes that are responsible for beam hardening, its effect on CT quantitation and image quality. The beam hardening correction mechanism that is built into the Inveon CT system by Siemens was studied thoroughly and was found to be lacking in several crucial aspects.

Firstly, the default set of coefficients were found be unsuitable for correcting for object sizes greater than ~30 mm diameter. Secondly, the manufacturer had completely overlooked the fact that the same set of default correction coefficients cannot be universally applied for all acquisition energies. The inherent problem was further compounded by the fact that, no information was provided regarding the set of acquisition conditions which were used by Siemens to generate the default coefficients in the first place.

From the preliminary investigations discussed in Sec 1.1, we establish that the maximum size of the object with which the default coefficients could achieve accurate BH correction was equivalent to an average mouse size. Subsequently, we have developed an independent methodology, based on linearization of CT projection data expanding the scope of BH correction in the system to larger rat-size equivalent objects (~71 mm). Just as significantly we generated BH coefficients for a set of 12 different acquisition settings.

The primary advantage of the approach is its simplicity of implementation. No prior knowledge of the incident spectrum is necessary. The accuracy of the approach largely depends on accuracy of determination of effective attenuation coefficient (μ_{eff}) for the imaged material for each kVp and filtration which is derived from the initial curvature of measured projection data R_{poly} as a function of material thickness.

The study is also significant in the realm of combined PET/CT studies where the CT image is utilized for attenuation correction of PET emission data. The process involves scaling of calculated attenuation coefficients at the effective x-ray energy in CT image to attenuation coefficients at the PET energy of 511 keV. Therefore, elimination of artifactual errors in CT images helps reduce potential quantitative errors in PET images as well.

Limitations of Approach

a) *Material Specificity* - A practical limitation of linearization is that it is specifically applicable to single-material objects [3][4]. It is important that the imaged object be of similar material composition and density as the calibration phantom. An added drawback is that it assumes homogenous materials for correction. Correction for multi-material objects with slightly differing densities would require a more complex iterative approach for BH correction. However, the methodology is well-suited to small animal imaging where the assumption of "single material object" closely approximated because bone volume is only a small percentage of the animal (approximately 5%) with the remaining tissue close to water-equivalent.

b) *Sensitivity to curvature of BH curve* – The method is highly sensitive to the curvature of polyenergetic CT data as a function of length of propagation. It was observed that the choice of the degree of polynomial to fit a BH curve strongly depends on the material density of the corresponding phantom. In case of materials like Delrin and Polyethylene [Fig. 7.2 and 7.3] whose densities are close to water, a third order polynomial works well. However, for correction of denser materials like aluminum, a much higher degree of polynomial fit is required [4].

c) Dependency of algorithm on scan acquisition conditions - The method is applicable for projection data acquired at the same acquisition conditions as the calibration phantom. For change in acquisition conditions, the system has to be recalibrated with a new calibration function.

d) Effect on Image Quality - Past studies have indicated an increase in ring artifacts after BH correction. This is because of the contrast enhancement that results from the projection of every point of the beam hardening curve towards the linear monoenergetic trendline [5]. Also, correction of BH artifacts, while improving upon the accuracy of quantitation, also leads to an increase in image noise, therefore decreasing the contrast-to-noise-ratio (CNR) [4] [5]. Hence a trade-off exists between quantitative and qualitative data. A possible solution to overcome this drawback would be the use of noise removal techniques on CT projection data, prior to reconstruction.

CHAPTER 9

CONCLUSIONS

The primary emphasis of this study was the implementation of BH corrections in the Inveon^{TM} CT for a range of different homogeneous materials and densities. Additionally, BH corrections for a number of different but common CT acquisition parameters were generated to fill a blatant void in the Inveon product offering.

The study also significantly expands our understanding of the characteristic and nature of beam hardening curve for water. The results are compared with solid materials of three different densities.

Secondly, we have exploited our understanding of the non-standard linearization based BH correction model built on the Inveon ^{TM} CT system, to develop a methodology to generate BH corrections that are compatible with the system. We developed a correction model based on linearization of original projection data. This pre-reconstruction procedure is fast, easy to apply and consistent with the existing implementation of BH correction on the Inveon ^{TM} CT. The accuracy of our proposed BH correction model has been demonstrated by artifact-free reconstructed CT images of water phantoms of diameters up to 71 mm. The correction scheme results in effective removal of the cupping artifact, which was observed when default correction coefficients provided by the manufacturer are applied.

The correction approach is also found to be effective for materials with densities near that of water. However for the BH correction in case of with high density materials like Aluminum , the Inveon system shows practical limitations for implementation.

In addition, since the accuracy of the method depends on the estimated linear attenuation coefficient of the phantom material the measurements made in this work will not be applicable to other voltage or pre-filtration settings. Keeping this in mind, the future scope of work could involve experiments by modifying the incident spectrum with different peak voltages and tube filtration settings and determination of optimal correction coefficients for each such combination.

BIBLIOGRAPHY

[1] G. T. Herman, "Correction for beam hardening in computed tomography," *Physics in Medicine and Biology, 24(1)*, pp. 81–106, 1979.

[2] K. Remeysen. and R. Swennen, "Beam hardening artifact reduction in microfocus computed tomography for improved quantitative coal characterization", *International Journal of Coal Geology,* 67, pp 101-111, 2006.

[3] R. Brooks and G. Di Chiro, "Beam Hardening in X-Ray ReconstructiveTomography," *Physics in Medicine and Biology, 21,* pp. 390-398, 1976.

[4] P. Hammersberg and M. Mangard, " Correction for beam hardening artefacts in computerised tomography", *Journal of X-Ray Science and Technology 8*, pp 75-93, 1998.

[5] E. Van de Casteele, "Model Based Approach for Beam Hardening Correction and Resolution Measurements in Microtomography", *Ph.D dissertation*, Universiteit Antwerpen, June 2004.

[6] International Commission on Radiation Units and Measurement. "Tissue substitutes in radiation dosimetry and measurement". *Bethesda, MD: ICRU Report 44*, 1989.

[7] H. Li, H. Zhang, Z. Tang, G. Hu, " Micro-computed Tomography for Small Animal Imaging: Technological Details", *Progress in Natural Science, 18*, pp. 513-521, 2008.

[8] G. Wang and M. Vannier, "Micro-CT scanners for biomedical applications: an overview," *Advanced Imaging, 16 (7)*, pp. 18–27, 2001.

[9] D.W Holdsworth and M.M Thornton, "Micro-CT in small animal and specimen imaging," *Trends in Biotechnology, vol. 20, no. 8*, pp. 34–39, 2002.

[10] J. L. Tremoleda et al. *EJNMMI Research*, pp 1-11, 2011.

[11] L. A. Feldkamp, L. C. Davis, and J. W. Kress, "Practical cone-beam algorithm", *J. Opt.   Soc. Am. A/Vol. 1, No. 6*, pp. 612-619, 1984.

[12] L.A. Feldkamp, S.A. Goldstein, A.M. Parfitt, et al., "The direct examination of three dimensional bone architecture in vitro by computed tomography", *J Bone Miner Res 4*, pp 3–11, 1989.

[13] Philippe C. Cattin, MIAC, *"Imaging Modalities: X- ray, CT, Fluoroscope"*, 2011.

[14] B.H Hasegawa, "The Physics of Medical X-ray Imaging", *2nd Edition. Madison, WI: Medical Physics Publishing*, *ISBN 0-94483-823-5*, 1991.

[15]   H. Turbell, Cone-Beam Reconstruction Using Filtered Backprojection. PhD thesis, *Dissertation No. 672, ISBN 91-7219-919-9*. Link¨oping University, Sweden, SE-581 83 Link¨oping, Sweden, February 2001.

[16]   G. Wang, T.H Lin, P. Cheng, D.M Shinozaki, "A General Cone – Beam Reconstruction Algorithm", *IEEE Transactions in Medical Imaging, 12 (3)*, pp 486-496,   1993.

[17]   Bruce D.Smith, "Image reconstruction from cone-beam projections: necessary and sufficient conditions and reconstruction methods", *IEEE Trans. Med. Imag. 4(1)*,1985.

[18]   Steven W. Smith, " The Scientist's and Engineer's Guide to Disgital Signal Processing" , 1st Edition*, ISBN-13:* 978-0966017632 , 1997.

[19]   H. K. Tuy, "An inversion formula for cone-beam reconstruction", SIAM J. Appl. Math., Vol.43, pp. 546-552 ,1983.

[20]   Z. Wei et. al, " Beam Hardening Correction for a Cone Beam CT System and its effect on spatial resolution", *Chinese Physics C(HEP & NP), 35(10)*, pp 978-985, 2011.

[21]   H. Gao et.al, "Beam Hardening Correction for Middle – Energy Industrial Computerized Tomography", *IEEE Transactions On Nuclear Science, 53 (5),* pp 2796-2807, 2006.

[22]   J. Deng, S. Yan, M.Chen, T. Bruckbauer, "Beam Hardening Correction Using a Conical Water-Equivalent Phantom for Preclinical Micro-CT", *IEEE Nuclear Science Symposium Conference Record*, pp 2922-2924, 2011

[23]   Resource Manual for Compliance Test Parameters of Diagnostic X-Ray Systems, Reprinted Jul, 1999.

[24]   Y. Wang, F. Wang, Z. Ou, "Modified FDK Algorithm for Cone-Beam Reconstruction with Efficient Weighting Scheme", *Proc. Of The Sixth World Congress on Intelligent Control and Automation, vol.2* pp 1- pp 35, 2006.

[25]   *Conditions for X-Ray Production*, Retrieved May 11, 2012 from http://whs.wsd.wednet.edu

[26]   J. Rowlands, "*Flat panel detectors for medical x-ray: Physics and Technology",* Available at   hepwww.rl.ac.uk/Vertex03/Talks/Row/Rowlands.pdf

[27]   N. M. Abbasi, *"The application of Fourier Analysis in solving the computed tomography (CT) Inverse Problem", 2010*

[28]   NIST X-Ray form factor, Attenuation and Scattering Tables (2012) , Retrived Aug'11 from http://physics.nist.gov/cgi-bin/ffast/chooseElement.pl?filename=form.html

[29]   Kirsten L. Boedeker et.al, " Emphysema: Effect of Reconstruction Algorithm on
        CT   Imaging Measures", *Radiology,* 232: pp 295–301, 2004.

[30]   S. Van, J. Deng, T. Bruckbauer, "A Conical Water-equivalent Phantom Design for
        Beam Hardening Corrections in Preclinical Micro-CT," 2011 PI2833US, Filed July
        29th, 2011.

[31]   J. Hsieh, "An Iterative Approach to the Beam Hardening Correction in Cone
        Beam CT," Med. Phys.,vol.27,pp23-29, 2000.

[32]   F. Jian, L. Hongnian , "Beam-hardening correction method based on original sinogram
        for X-CT", *Nuclear Instruments and Methods in Physics Research A ,* 556,
        pp 379 -385, 2006.

[33]   S. Krimmel, et al., *Nuclear Instruments and Methods in Physics Research A ,*542
        pp 399, 2005.

[34]   De Man et al, "An Iterative Maximum-Likelihood Polychromatic Algorithm for CT*",
        IEEE Trans. Med. Imag*., vol.20 (10), pp 999-1008, 2001.

[35]   M. Grass, T. Köhler, and R. Proksa, "3D cone-beam CT reconstruction for
        circular trajectories," *Phys. Med. Biol*., vol. 45, pp. 329-347, 2000.

[36]   X. Tang and R. Ning, "A cone beam filtered backprojection (CB-FBP)
        reconstruction algorithm for a circle-plus-two-arc orbit," *Med. Phys*.,
        vol. 28, no. 6, pp. 1042-1055, 2001.

[37]   F. Earnest, E. C. McCullough, and D. A. Frank, "Fact or artifact: An analysis of artifact
        in high-resolution computed tomographic scanning of the Sella," *Radiology*, vol. 140,
        pp. 109–113, 1981.